https://doi.org/10.5194/egusphere-2025-3630
Preprint. Discussion started: 10 October 2025

Satellite-Based Extension of the Soil Freezing Curve Paradigm: Detecting Extrinsic Freeze/Thaw Thresholds with SMAP in Mid-Latitudinal Agricultural Fields

Renato Pardo Lara[1], Andreas Colliander[2], Erica Tetlock[3], Jarret Powers[4], Jaison Ambadan[1], and Aaron Berg[1]

[1]Department of Geography, Environment and Geomatics, University of Guelph, 50 Stone Rd. E., Guelph, J8N 0K6, Ontario, Canada
[2]Jet Propulsion Laboratory, California Institute of Technology, 4800 Oak Grove Drive, Pasadena, 91109, California, USA
[3]Environment and Climate Change Canada, 11 Innovation Blvd., Saskatoon, S7N 3H5, Saskatchewan, Canada
[4]Agriculture and Agri-Food Canada, 303 Main St, Winnipeg, R3C 3G7, Manitoba, Canada

Correspondence: Renato Pardo Lara (rpardo@uoguelph.ca)

Abstract.

We present a novel method for surface freeze/thaw (F/T) classification based on L-band brightness temperature (T_B), as measured by the Soil Moisture Active Passive (SMAP) mission, combined with thermodynamic temperature estimates, whether in situ or derived from near real-time model output. Variations in the cryosphere have significant, lasting impacts on physical, biological, and social systems, and act as sensitive indicators of climate change. Remote sensing at microwave frequencies is uniquely suited for monitoring the cryosphere's spatial and temporal dynamics. Indeed, SMAP was tasked with providing a daily classification of the surface F/T state as one of two primary mission goals. Although surface F/T events are extrinsically driven phenomena, most existing classification algorithms rely on intrinsic thresholds—those derived from single-variable observables—that may not accurately reflect in situ conditions. Meanwhile, soil physicists have long used a robust framework to study the relationship between unfrozen water content and sub-freezing temperature, known as the soil freezing characteristic curve (SFC). These curves, and to a lesser extent their soil thawing characteristic curve (STC) branches, have been well studied in laboratory settings using a variety of instruments and methods. These concepts have not been extended to remote sensing (RS) until now.

The remotely sensed surface freezing characteristic curves (SurFCs) introduced here are the satellite-pixel-scale counterpart to SFCs. SurFCs are constructed with SMAP T_B measurements, which are inversely correlated with water content, along with thermodynamic temperature records at two mid-latitude sites. We used in situ temperature data from SMAP core validation sites near Kenaston, Saskatchewan and Carman, Manitoba, covering a combined total of nine years, alongside modelled temperature estimates from the Goddard Earth Observing System Model, Version 5 Forward Processing product (GEOS-5 FP). SurFCs constructed with in situ soil temperatures showed a structure like that of SFCs, including analogue thawing branches, identified as surface thawing characteristic curves (SurTCs). Lastly, we show SurTCs can serve as a tool for identifying extrinsic thresholds—transition points linked to both the system's physical state and its external drivers —enhancing the realism and

https://doi.org/10.5194/egusphere-2025-3630
Preprint. Discussion started: 10 October 2025

operational accuracy of satellite-based F/T classification. Overall, the proposed ${T_B}^H{}_{\min}$ approach improved detection accuracy by 39.4 % compared to the widely used normalized polarization ratio (NPR) method.

This analysis challenges the prevailing assumption that 0.15 °C is a universal F/T threshold. Instead, we argue that the threshold should be determined from measurements of the system's physical response and environmental forcing (SurFC/SurTC). Although useful, a 0.15 °C classifier is not uniformly applicable across freeze–thaw phenomena or measurement methods.

1 Introduction

Frozen ground is the single largest component of the cryosphere by area, with over one-third of Earth's land surface undergoing seasonal transitions between frozen and thawed states (Barry and Gan, 2011). These freeze/thaw (F/T) events critically affect terrestrial water, carbon, and energy budgets. For example, soil F/T cycles alter key hydrological processes (evaporation, runoff, infiltration, soil moisture dynamics, groundwater recharge, and stream flow generation) and influence biogeochemical and ecological processes such as soil erosion and microbial respiration (Andersland et al., 1996; Andersland and Ladanyi, 1994; Christensen et al., 2013; He and Dyck, 2013; Koponen and Martikainen, 2004; Öquist et al., 2009; Tilston et al., 2010; Wagner-Riddle et al., 2017; Flerchinger et al., 2005). Spatiotemporal changes in surface F/T phenomena therefore have important socio-economic implications for water futures, forest and agricultural productivity, flood risk, and climate feedbacks. However, the vast extent of frozen ground, coupled with its prevalence in remote, climatically extreme regions, presents difficulties for monitoring F/T patterns using traditional in situ measurements (Dunbar et al., 2020; Derksen et al., 2017). These challenges motivate the use of remote sensing approaches for large-scale F/T monitoring.

Remote sensing (RS) at microwave (μw) frequencies ($1-1000$ GHz) is uniquely positioned for observing global cryospheric changes. In this region of the electromagnetic (EM) spectrum, the solar radiation is minimal, allowing passive sensors, like radiometers, to detect the Earth's own thermal emission. These sensors report measurements as brightness temperature (T_B), which is the blackbody temperature required to produce the observed microwave radiance, according to Planck's law (Ulaby et al., 1981; Rees, 2001). Because real surfaces are not perfect black bodies, the measured T_B depends primarily on two factors: the material's physical, or thermodynamic, temperature and the efficiency of its emission, or emissivity (Jones et al., 2010). Emissivity, in turn, is governed by the dielectric properties of surface materials in our case, soil moisture, ice content, surface roughness, and vegetation cover.

At L-band ($1-2$ GHz, depending on the definition), microwave emission is particularly sensitive to changes in soil moisture and its F/T state due to the stark contrast in permittivity between liquid H_2O ($\varepsilon_{\text{liquid } H_2O} \sim 80$) and solid ice ($\varepsilon_{\text{frozen } H_2O} \sim 5$. As a result, changes in L-band polarized brightness temperature (${T_B}^P$) indirectly reflect changes in near-surface soil moisture content and phase state (Schmugge et al., 2002; Rautiainen et al., 2012). Emission with the electric field parallel to the Earth's surface is measured as horizontally polarized brightness temperature (${T_B}^H$), whereas a perpendicular orientation relative to Earth's surface yields vertically polarized brightness temperature (vertically polarized brightness temperature (${T_B}^V$)), (Ulaby et al., 1981). These two polarizations respond differently to surface conditions. ${T_B}^H$ is typically more sensitive to surface roughness and moisture in the uppermost soil layers, while ${T_B}^V$ can better penetrate through shallow vegetation or snow

https://doi.org/10.5194/egusphere-2025-3630
Preprint. Discussion started: 10 October 2025

cover (Njoku et al., 2003; Royer et al., 2017). The difference between ${T_B}^H$ and ${T_B}^V$ is often quantified by the normalized polarization ratio (NPR), defined as

$$NPR = \frac{|T_B^H - T_B^V|}{T_B^H + T_B^V} \quad (1)$$

This ratio accentuates the contrast between frozen and thawed conditions. Even a small amount of liquid water (e.g., during a snowmelt) will sharply lower the surface emissivity and cause a notable change in NPR (Derksen et al., 2000; Rautiainen et al., 2012; Roy et al., 2015). Indeed, NPR-based thresholding underpins operational algorithms for detecting snowmelt and soil F/T transitions in many F/T detection products, including those from Soil Moisture Active Passive (SMAP) and Soil Moisture and Ocean Salinity (SMOS) missions (Kim et al., 2017; Entekhabi et al., 2010; Kerr et al., 2017). The main advantage of using threshold-based polarization ratios like NPR is pragmatic in nature; they provide the highest accuracy for surface F/T discrimination (Rautiainen et al., 2016; Roy et al., 2015). However, these intrinsic thresholds are not directly tied to the physical drivers of freezing or thawing.

Meanwhile, decades of soil physics research have shown that liquid H_2O can persist in freezing soils at temperatures as low as –80 °C, due to capillary, adsorptive, and osmotic forces (Bouyoucos and McCool, 1915; Mousson, 1858). The relationship between a soil's unfrozen water content and sub-freezing temperature is known as the soil freezing characteristic curve (SFC) and is a fundamental property of the physical processes involved in soil moisture F/T phenomena (Ireson et al., 2013). It is well documented that this relationship exhibits hysteretic behaviour when frozen soil thaws, leading to the definition of the soil thawing characteristic curve (STC; Zhou et al., 2019; Hu et al., 2020; Pardo Lara et al., 2021). The SFC paradigm can be used to understand the transport of heat, H_2O, and solutes in frozen soils (Koopmans and Miller, 1966). This versatile tool has also been used to estimate the hydraulic conductivity function of partially frozen soils (Azmatch et al., 2012) and to investigate water and solute transport and redistribution in soil during winter (Spaans and Baker, 1996). SFCs have been well studied in laboratory settings using a variety of instrumentation and methods, including dilatometers, calorimeters, tensiometers, heat capacity, X-ray diffraction, nuclear magnetic resonance, and various EM soil moisture probes (Cheng et al., 2014; Koopmans and Miller, 1966; Mavrovic et al., 2021; Pardo Lara et al., 2021, 2020; Tian et al., 2018; Wen et al., 2012; Yoshikawa and Overduin, 2005). However, the SFC paradigm and the concomitant STC have not yet been applied to remote sensing observations of landscapes.

In this study, we extend the SFC paradigm to satellite-scale observations and evaluate its utility for freeze–thaw classification. We specifically test four hypothesis:

1. Remotely sensed ${T_B}^P$ and in situ soil temperature can be used to construct brightness temperature–derived surface freezing and thawing characteristic curves (T_B-SurFCCs and T_B-SurTCCs, hereafter SurFCs and SurTCs for brevity) at the scale of the footprint of passive microwave satellites;

2. Remotely sensed T_B and modelled thermodynamic temperature can be used to produce SurFCs and SurTCs at the satellite scale;

https://doi.org/10.5194/egusphere-2025-3630
Preprint. Discussion started: 10 October 2025

3. SurTCs can be used to identify an extrinsic threshold for surface F/T state classification, and

4. In a remote sensing context, SurTCs can serve as a tool for F/T product validation.

We anticipate that incorporating these SurFC/SurTC-based insights will improve F/T detection and validation methods. The remainder of this paper is organized as follows. Section 2 describes the study sites, data sets and methodology for F/T classification and analysis. Section 3 presents results, including examples of SurFCs/SurTCs derived from both in situ and modelled temperature data. In Section 4, we discuss the implications of these results, compare them with previous studies, and examine limitations. Finally, Section 5 offers our conclusions and recommendations for future work.

2 Data Sources and Methods

In these sections, we review the SMAP satellite F/T products, ancillary data sets, in situ measurements, and the methods used to produce and analyze the proposed SurFCs and SurTCs.

2.1 SMAP data products

Launched in January 2015, the SMAP satellite mission originally provided radar (active) and radiometer (passive) L-band observations of Earth's surface. The SMAP spacecraft is in a 685-km circular, sun-synchronous orbit with equator crossings at about 6 a.m. and 6 p.m. local time with a look angle of 40°. The real-aperture swath width of 1000 km provides global coverage within 3 days or less equatorward of 35°N/S and 2 days poleward of 55°N/S. The SMAP radar lost its transmitting function in July 2015. The radiometer continues to operate, providing L-band radiometer observations in vertical (V) and horizontal (H) polarizations at 1.41 GHz (Piepmeier et al., 2017). Space-borne radiometers, like SMAP's passive component, are uniquely positioned to map large-scale patterns and daily variations in terrestrial F/T cycles state at the temporal and spatial resolution coverage needed for global land hydrology applications (Entekhabi et al., 2010; Kim et al., 2011). SMAP data are resampled to a global, cylindrical 36 km Equal-Area Scalable Earth Grid, Version 2.0 (EASE-Grid 2.0; Brodzik et al., 2012, 2014). This study focuses on the descending overpass data at about 6 a.m. local time, a time when the soil and overlying vegetation temperatures are at near isothermal conditions which allows simplification of the radiative transfer model at the core of the retrieval algorithm.

2.1.1 Brightness temperature (T_B)

In this study, the SMAP T_B measurements at a spatial resolution of 36^2 km^2 contained in the SMAP Level 3 Radiometer Global Daily 36 km EASE-Grid Freeze/Thaw State Product, Version 3, (L3_FT_P) were analyzed (Xu et al., 2020). The L3_FT_P product provides a composite of daily estimates of global land surface conditions retrieved by the SMAP passive microwave radiometer. The T_B data are the calibrated, geolocated, time-ordered mean of fore/aft views of the 360° antenna scan processed within an EASE-Grid 2.0 polar and cylindrical projection format. Note that the L3_FT_P product provides $T_B^{V,H}$ at the Earth's surface. The SMAP radiometer provides measurements of T_B with better than 1.3 K uncertainty (1-sigma; O'Neill et al.,

https://doi.org/10.5194/egusphere-2025-3630
Preprint. Discussion started: 10 October 2025

2021; Piepmeier et al., 2017). Since the ${T_B}^P$ difference across the dynamic range of surface soil moisture can be many tens of K ($\gtrsim$ 70 K), the L-band radiometer is a highly sensitive indicator of surface soil moisture F/T state. In this study, we focus on H-polarized T_B as it displayed the largest amplitude variations (Lv et al., 2022).

2.1.2 Surface F/T classification

The L3_FT_P provides a daily classification of the F/T state for land areas derived from the mission's L-band radiometer. The F/T classification algorithm is based on the $T_B^{V,H}$ time series response to the change in permittivity of the land surface associated with H_2O transitioning between solid and liquid phases (Dunbar et al., 2020). While other F/T algorithmic approaches are possible (for example, moving window; temporal edge detection) these techniques do not fulfill the SMAP data latency requirement (within 24 hours of acquisition for L2 products and within 50 hours for L3 products). This method examines the time series progression of the remote sensing signature relative to signatures acquired during seasonal reference frozen and thawed states, making it part of the seasonal thresholds algorithm (STA) family. At L-band frequencies, Rautiainen et al. (2014) showed T_B increase at horizontal (${T_B}^H$) and vertical (${T_B}^V$) polarizations while their difference ($\mid {T_B}^V - {T_B}^H \mid$) decreases when soil moisture freezes. The change in the T_B difference is independent of the change in the physical temperature, it depends only on the permittivity and was, therefore, employed in the retrieval algorithm after normalizing it with the sum of the polarization yielding the NPR, defined earlier in Equation 1.

The frost factor, $FF_{\text{NPR}}(t)$, is then defined for an observation acquired at time t as:

$$FF_{\text{NPR}}(t) = \frac{NPR(t) - NPR_{\text{FR}}}{NPR_{\text{TH}} - NPR_{\text{FR}}} \tag{2}$$

where, $NPR(t)$ is the NPR calculated at time t, for which a F/T classification is sought, and NPR_{TH} and NPR_{FR} are the reference thawed and frozen NPR values, respectively. Decreases and increases in FF_{NPR} are associated with landscape freezing and thawing transitions, respectively, with the decrease in FF_{NPR} under frozen conditions the result of small increases in the V-pol T_B combined with larger increases at H-pol (Rautiainen et al., 2014). A threshold level, Δ, is then defined such that

$$FF_{\text{NPR}}(t) < \Delta \implies \text{frozen} \tag{3}$$

$$FF_{\text{NPR}}(t) \geq \Delta \implies \text{thawed} \tag{4}$$

The threshold can vary between 0 and 1. In other words, the algorithm evenly splits the difference of the frozen and thawed references, adding the result to the frozen reference to account for its offset, to define a threshold value for surface F/T discrimination. For SMAP L3_FT_P the parameter Δ is fixed at 0.5 across the entire F/T domain. We invert Equation 2 to solve for the NPR at that particular Δ value. That is to say

$$NPR_{\text{threshold}} = \Delta(NPR_{\text{TH}} - NPR_{\text{FR}}) + NPR_{\text{FR}} \tag{5}$$

The equations above are run on a grid cell-by-cell basis for unmasked portions of the F/T domain. The output is a binary state variable designating frozen or thawed conditions for each unmasked grid cell. Various studies have shown the NPR to

https://doi.org/10.5194/egusphere-2025-3630
Preprint. Discussion started: 10 October 2025

be preferred over other approaches as it minimizes sensitivity to physical temperature and outperforms other L-band brightness temperature-based approaches (Rautiainen et al., 2014; Roy et al., 2015). The NPR is most effective in areas with low to moderate vegetation cover, while NPR signal-to-noise is lower in dense vegetation areas (e.g., forests) due to more diffuse scattering of microwave emissions and reduced differences between ${T_B}^H$ and ${T_B}^V$ (e.g., Wigneron et al., 1995). For lower latitudes or conditions where the NPR algorithm requirements are not met, which excludes our study areas, a modified seasonal thresholds algorithm (MSTA) using the single-channel vertically polarized brightness temperature algorithm (FT-SCV) is employed. In the FT-SCV algorithm, the measured ${T_B}^V$ is correlated with surface air temperatures, from global weather stations and reanalysis data, to identify frozen and non-frozen references based on the freezing point of H_2O (Kim et al., 2017; Podest et al., 2014).

2.1.3 Ancillary SMAP data: GEOS-5 FP T_{eff}

The SMAP L3 Radiometer Global Daily 36^2 km^2 EASE-Grid Soil Moisture, Version 8 product, L3_SM_P, uses ancillary data including soil temperature information. The Choudhury and Schmugge (1982) two-layer approach for T_{eff}, which combines estimates of a "surface" temperature and a "deep" temperature using a proportional coefficient, C, dependent on the microwave wavelength, has been used in all previous SMAP data releases and by other missions with good success (O'neill et al., 2021). A modified formulation of the model, Equation 6, resulted in good agreement between the in situ soil moisture data and the retrieved soil moisture,

$$T_{\text{eff}} = K \times [T_{\text{soil 2}} + C(T_{\text{soil 1}} - T_{\text{soil 2}})] \tag{6}$$

where, $T_{\text{soil 1}}$ refers to the average soil temperature for the first soil layer (5-15 cm) and $T_{\text{soil 2}}$ refers to the average soil temperature for the second soil layer (15-35 cm) of the NASA Global Model and Assimilation Office (GMAO)'s global Numerical Weather Prediction (NWP) system, the Goddard Earth Observing System Model, Version 5 Forward Processing product (GEOS-5 FP) land surface model, at their native 0.25 x 0.3125-deg grids. K is a factor included to address the observed bias between ancillary modelled soil temperature and measured in situ temperature at core validation sites and sparse network stations. Such structural biases are inevitable given the fact that they are parameterized and the result of numerical models as well as because the model grids (in the horizontal) are often tens of kilometres which span large heterogeneities in landscape conditions like slope, aspect, land use, and soil texture. For a microwave wavelength of 21 cm Choudhury and Schmugge (1982) report that $C = 0.246$, while O'neill et al. (2021) report $K = 1.007$ for SMAP.

The SMAP bias correction was factored out of the ancillary effective soil temperature product, as we are interested in the ground temperature, unaffected by structural biases as captured by the satellite. The GEOS-5 FP geophysical data are derived at a resolution of 36^2 km^2 and posted on the EASE-Grid 2.0 with 36-km spacing. We utilized the NASA SMAP Level-2 ancillary surface temperature from the GEOS-5 FP model. GEOS-5 FP is a global NWP and data assimilation system that produces NRT surface and soil temperature estimates with approximately 10–12 hour latency, demonstrating operational potential for rapid F/T state mapping. These temperature fields, derived at ~0.25°resolution, are used operationally in SMAP retrieval algorithms as ancillary inputs. In our study, we use archived GEOS-5 FP surface temperature data retrospectively; however, because this

https://doi.org/10.5194/egusphere-2025-3630
Preprint. Discussion started: 10 October 2025

is an operational forward-processing product—not a delayed reanalysis—our analysis also serves as a proof-of-concept that the same approach could support NRT or even short-range forecast applications in F/T mapping. Holmes et al. (2012) found an RMSE of 1.6 K when comparing GEOS-5 FP T_{eff} to in situ measurements of the Oklahoma Mesonet and this serves as our uncertainty estimate for the product.

2.2 GlobSnow near-real-time Snow Water Equivalent dataset

To investigate environmentally driven underperformance, we also used snow estimates from the daily GlobSnow Level 3 snow water equivalent (SWE) version 1.0 product. This product is part of operational near real-time (NRT) snow information service maintained by the GlobSnow Consortium, coordinated by Finnish Meteorological Institute (FMI) and funded by the European Space Agency (ESA). The NRT service initiated operations on October 2010. Historical datasets and NRT products are available for SWE and snow extent over the northern hemisphere, covering all land surface areas with the exception of mountainous regions and Greenland, to the GlobSnow user community through this website.

For product version 1.0, the basis for SWE retrieval methodology, presented in (Pulliainen, 2006), is complemented with a time series melt-detection algorithm (Takala et al., 2009). The two algorithms are combined to produce snow water equivalent maps incorporated with information on the extent of snow cover on coarse resolution (25 x 25 km grid cells). The passive microwave observations and weather station observations European Centre for Medium-Range Weather Forecasts (ECMWF) are collected in an assimilation scheme to produce maps of SWE estimates (in EASE-Grid format).

This approach was selected by ESA as the baseline method for the Global Snow Monitoring for Climate Research. For this product,SWE describes the depth of liquid water, in mm, in the snow pack that would be formed if the it completely melted. The GlobSnow method provides the most reliable existing observation-based (satellite plus in situ) estimates of the hemispheric-scale snow mass (SWE).

2.3 In situ measurements

The baseline science mission requirements specific to terrestrial F/T science activities state that SMAP shall provide estimates of surface binary F/T state for the region north of 45°N latitude, which includes the boreal forest zone, with a mean spatial classification accuracy of 80% at 3 km spatial resolution and 2-day average intervals. The minimum mission requirement accuracy is 70%. Validation is defined as the process of assessing by independent means the quality of the data products derived from the system outputs (Colliander, 2014). SMAP utilizes a wide range of methodologies in validating the mission science products, which include in situ networks, other satellite products, and model-based products (Jackson et al., 2012). As outlined in the SMAP mission calibration and validation plan the accuracy of the SMAP surface F/T product is primarily determined through comparisons against in situ surface F/T classifications based on temperature measurements discriminated against a 0.15 °C (Jackson et al., 2012), hereafter referred to as the current “gold standard” F/T test.

The highest priority in situ resources for SMAP F/T cal/val are the CVSs (Derksen et al., 2017). These sites provide in situ observations that can be used to estimate soil moisture F/T, among others, at the spatial resolution of the SMAP geophysical data products. Ideally, these sites include reference air temperature (2 m height), as well as vegetation (stem and canopy) and

https://doi.org/10.5194/egusphere-2025-3630
Preprint. Discussion started: 10 October 2025

surface (<5 cm depth) soil temperature measurements with high temporal fidelity (daily or better) sampling and representation over the observed range of climate, terrain, land cover and vegetation biomass conditions. The SMAP validation plan identifies five potential CVSs for SMAP surface F/T product. These include the Kenaston Soil Moisture Network (KSMN) in Saskatchewan, Canada (Tetlock et al., 2019) and Real-Time In-Situ Soil Monitoring for Agriculture (RISMA) network within Manitoba, Canada (Bhuiyan et al., 2018; Rowlandson et al., 2018) as shown in Figure 1. The KSMN and RISMA network are dense networks that provide multiple sampling sites within a spatial domain matching SMAP's product pixel footprint. These sites are within flat agricultural landscapes underlaid by mineral soil, making them a unique testing ground for the construction of SurFCs at the satellite scale. For our study, at the KSMN, soil temperature at 2.5 cm in depth was measured with Campbell Scientific T109 thermistors, which have an uncertainty of ± 0.2 °C according to the manufacturer. The air temperature at 2 m was measured with Campbell Scientific HMP45C temperature probes with an uncertainty, dependent on temperature, of up to ± 0.5 °C in the ranges seen. In situ soil temperature measurements at a depth of 5 cm come from Stevens HydraProbe (HP) II SDI-12 sensors horizontally installed into the soil profile at a depth 5 cm (CVS standard depth) which have an instrumental uncertainty of ± 0.5 °C (Pardo Lara et al., 2020, 2021). To investigate the environmentally driven underperformance observed in the results, we also examined precipitation measurements (in mm) collected at all RISMA stations using a Hydrological Services TB4 tipping bucket rain gauge mounted at a height of 2.5 m.

https://doi.org/10.5194/egusphere-2025-3630
Preprint. Discussion started: 10 October 2025

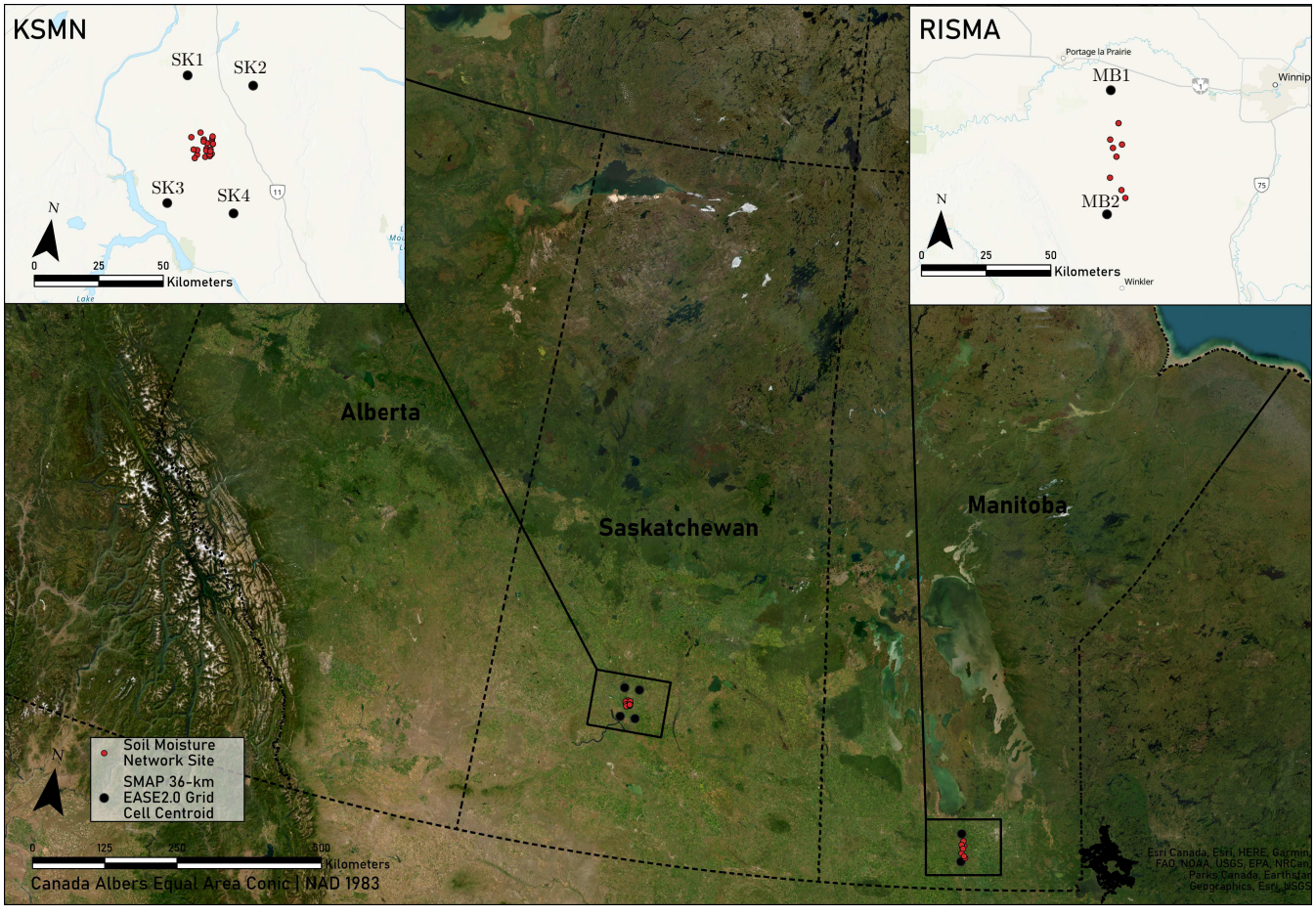

Figure 1. Map of the Saskatchewan and Manitoba study areas. Black dots mark SMAP pixel centroids, and red dots mark in situ network stations (KSMN in Saskatchewan and RISMA in Manitoba), which together define the core validation sites for this study.

https://doi.org/10.5194/egusphere-2025-3630
Preprint. Discussion started: 10 October 2025

Table 1: List of SMAP pixels and the soil moisture network stations located within them, along with their coordinates, available instrumentation, and soil texture. Instruments include the Stevens HydraProbe (HP), Campbell Scientific T109 thermistors (T109), and Campbell Scientific HMP45C temperature/relative humidity probes (HMP45C).

SMAP Pixel	Network	Latitude	Longitude	Instruments	Sand	Silt	Clay
SK1 (*Centroid*)		51.638	−106.618				
	KSMN	51.449	−106.496	1 HP, T109, HMP45C	25.4	56.3	18.2
		51.416	−106.450	1 HP	26.0	51.0	23.0
		51.427	−106.472	1 HP	13.8	57.0	29.2
		51.420	−106.472	1 HP	30.2	51.3	18.5
		51.428	−106.543	1 HP	31.8	46.1	22.1
SK2 (*Centroid*)		51.189	−106.618				
	KSMN	51.368	−106.449	1 HP	37.0	41.0	22.0
		51.371	−106.496	1 HP	34.0	50.0	16.0
		51.387	−106.499	1 HP	42.0	41.0	17.0
		51.387	−106.520	1 HP	39.0	44.0	17.0
		51.397	−106.449	1 HP	26.6	55.7	17.7
		51.390	−106.449	1 HP	26.0	50.0	24.0
		51.358	−106.506	1 HP	50.0	32.0	18.0
SK3 (*Centroid*)		51.638	−106.245				
	KSMN	51.416	−106.418	1 HP	29.0	49.0	22.0
		51.426	−106.426	1 HP, T109, HMP45C	26.8	51.4	21.8
		51.417	−106.418	1 HP	20.0	43.0	37.0
		51.437	−106.426	1 HP, T109, HMP45C	12.7	70.1	17.2
		51.442	−106.426	1 HP	24.6	59.5	15.9
SK4 (*Centroid*)		51.189	−106.245				
	KSMN	51.382	−106.416	1 HP	26.2	60.5	13.3
		51.373	−106.425	1 HP	28.6	57.3	14.1
		51.378	−106.426	1 HP	28.0	59.0	13.0
		51.396	−106.426	1 HP	31.0	46.0	23.0
		51.390	−106.426	1 HP	15.7	52.0	32.3

Continued on next page

https://doi.org/10.5194/egusphere-2025-3630
Preprint. Discussion started: 10 October 2025

Table 1 (continued).

SMAP Pixel	Network	Latitude	Longitude	Instruments	Sand	Silt	Clay
MB1 (*Centroid*)		49.867	–98.029				
	RISMA	49.679	–97.960	3 HP	3.7	24.6	71.7
		49.666	–98.008	3 HP	78.3	9.2	12.5
		49.753	–97.982	3 HP	3.6	33.2	63.2
		49.695	–98.024	3 HP	81.3	6.0	12.7
MB2 (*Centroid*)		49.434	–98.029				
	RISMA	49.562	–98.019	3 HP	78.8	10.1	11.1
		49.493	–97.934	3 HP	44.9	20.8	34.3
		49.520	–97.956	3 HP	47.1	21.1	31.8
		49.636	–97.988	3 HP	90.4	0.2	9.4

2.4 Methods

The signature acquired at thermal microwave frequencies represents a sampling of the aggregate landscape (relative) permittivity and structural characteristics (shapes, sizes, and spatial arrangement; Entekhabi et al., 2010; McDonald and Kimball, 2005). In terms of permittivity, there is a large contrast between liquid ($\varepsilon_r \sim 80$) and frozen H_2O ($\varepsilon_r \sim 5$). As soil moisture freezes, the molecules become bound in a crystal lattice, impeding their free rotation, increasing in volume and decreasing their density, and increasing the porosity of the soil, thus reducing the permittivity. However, low permittivities are not uniquely associated with frozen soil, dry soil has similar permittivity values to frozen soil. Indeed, if there is no soil moisture, there is practically no electrically observable change between frozen and thawed soil moisture states.

At present, partially due to a lack of appropriate permittivity models, the identification of surface H_2O F/T state of the upper soil layer is conducted with the use of the empirical models for T_B registered by remote sensing satellites (Rautiainen et al., 2016; Xu et al., 2016). Thus far, methods have primarily relied on passive microwave radiometry in the L-, K-, and Ka-bands to infer surface F/T state through their sensitivity to changes in the soil permittivity. In this section we discuss the construction of SurFCs and SurTCs using T_B measurements as a proxy for water content, how to identify a data-driven dynamic threshold for surface F/T classification, and present statistical approaches for comparing the binary classification stemming from this threshold against other methods.

2.4.1 Constructing SurFCs and separating SurTCs

The datasets were temporally and spatially collocated with the corresponding SMAP observations and pixels, based on proximity and Euclidean distance, respectively. The in situ measurement frequency was 30 minutes or less, meaning the time

https://doi.org/10.5194/egusphere-2025-3630
Preprint. Discussion started: 10 October 2025

difference between the SMAP overpass and selected measurement was approximately 15 minutes. When data was available from multiple stations within the SMAP pixel, we averaged multiple measurements and calculated the standard deviation to capture some of the field variability. When this deviation was larger than the network's instrumental uncertainty (± 0.5 °C) the former was used as the measurement uncertainty. Similar to Dunbar et al. (2020) and Salmabadi et al. (Under Review), only data acquired at temperatures $\leq$ 5 °C were included for these analyses.

The SurFC was constructed by plotting the remotely sensed ${T_B}^H$ and NPR values in the ordinate against the in situ or forecast temperature of choice (i.e., air temperature or soil temperature) in the abscissa. We chose the horizontally polarized T_B due to its greater dynamic range, attributed to the difference in the reflection and transmission of EM radiation at the air-surface interface for each polarization and possible impedance matching along with refraction effects (Rautiainen et al., 2014). However, since there is a negative correlation between T_B and soil moisture content, the shape of the SurFC is a reflection on the x-axis of the more familiar SFC. To compensate for this, the SurFCs are transformed by inverting the y-axis. The plotted values were connected temporally, to give a sense of the progression around regions of interest.

2.4.2 Data-driven surface freeze/thaw (F/T) threshold

We propose the dip in T_B, captured by the minimum ${T_B}^H$, as a relatively simple, yet efficient surface F/T classification feature since it corresponds to a wet snow signal during the seasonal snow melt.

The diurnal amplitude variation (DAV) in brightness temperature between the morning and the evening overpasses is a method for snowmelt detection, originally developed with coarser resolution passive microwave products in a glaciated environments (Ramage and Isacks, 2002). DAV is smaller during both the coldest winter months and snow-off periods than during melt events. Notably, DAV continues to increase with more cycles of melt-refreeze, due to continued snowpack metamorphism. Therefore, refreezing causes the brightness temperature to drop below the previous cold, dry state due to enhanced scattering from grain metamorphism (Johnson et al., 2020).

During the seasonal melt in snow dominated watersheds, the higher emissivity from liquid water near the snow surface rapidly increases the observed passive microwave T_B. Melt and freeze cycles cause snow grain size to increase, which further attenuates the passive microwave signal, causing much lower T_B values for a refrozen snowpack as opposed to a dry winter snowpack that has never melted (Burke et al., 1984). Studies have also shown that increased stream discharge either coincides with or directly follows the end of the high DAV period in snow-dominated watersheds (Kopczynski et al., 2008; Ramage et al., 2006; Vuyovich and Jacobs, 2011).

Since the T_B of a wet snow pack drops below that of a dry winter snowpack and grain metamorphism associated with F/T events causes it to drop below the previous state, we attribute the minimum T_B to the wet snow signal associated with the spring melt. Therefore, when a snowpack is present, we link the scene featuring the minimum ${T_B}^H$ to the seasonal snow melt and concomitant soil moisture state change.

We constrain the search to a thermodynamic temperature window of $\pm$ 5 °C to scope out the relevant phenomena, as done in the FT-SCV SMAP surface F/T algorithm (Dunbar et al., 2020). Once the minimum ${T_B}^H$ value is found within that temperature range, the associated temperature is considered the F/T discriminator. As discussed more in-depth in Section 4.4, a

https://doi.org/10.5194/egusphere-2025-3630
Preprint. Discussion started: 10 October 2025

data-driven threshold is desirable given the measurement mismatch between the SMAP radiometer and the average temperature measurements at 5 cm in depth, as well as other confounding factors such as freezing point depression.

2.4.3 Classification statistics

In essence, surface F/T classification can be reduced to the question, "is the soil moisture frozen?" Where the null hypothesis is that the soil moisture is not frozen and a "gold standard" classification methodology is the reference. Type I errors are false positives, where the scene is identified as frozen when it is not. Type II errors are false negatives, where the scene is not identified as frozen when it is, in fact, frozen. We report the freezing scene prevalence (proportion of times a pixel is found to be frozen), the accuracy, the recall or sensitivity (proportion of times the classification is correct for frozen pixels), and the precision (how often the model gets the prediction right).

The F_1-score is also provided which measures a classifier's accuracy by taking the harmonic mean of the precision and the recall, allowing us to consider the so-called positive predictions (false negatives, false positives, and true positives) in one statistic. The F_1-score assumes that both variables are drawn from the same distribution and thus have the same expected prevalence. The precision and the F_1-score are intrinsically unidirectional, aiming to assess the deductive effectiveness of predictions in the direction proposed by a rule, theory, or classifier. We also highlight the negative likelihood ratio (LR^-), which is defined as how many times more likely a false negative (Type II error) is than a true negative classification, based on in situ measurements. This last statistic is calculated by dividing the false negative rate by the true negative rate.

In short, statistical measures of the performance of a classification test included overall accuracy and per-pixel precision, recall, LR^-, and F_1-score. The statistical equations for these metrics are as follows:

$$\text{Overall Accuracy} = TP + TN/(TP + FP + TN + FN) \tag{7}$$

$$\text{Precision} = TP/(TP + FP) \tag{8}$$

$$\text{Recall} = TP/(TP + FN) \tag{9}$$

$$F_1\text{-score} = 2 \times \text{Precision} \times \text{Recall}/(\text{Precision} + \text{Recall}) \tag{10}$$

$$\mathrm{LR}^- = FN_{\text{rate}}/TN_{\text{rate}} = [FN/(FN + TP)]/[TN/(TN + FP)] \tag{11}$$

where, TP are true positives (correct hit), FP false positives (false alarm), FN false negatives (miss), and TN are true negatives (correct no alarm). F_1-score is the harmonic mean of precision and recall.

3 Results

In this section we present the results from applying our methods on the curated data set.

3.1 SurFCs and SurTCs from in situ temperature sources

There are six SMAP pixels encompassing the University of Guelph/Environment and Climate Change Canada soil monitoring stations at the KSMN. Four of those pixels were analyzed by Pardo Lara et al. (2020) and are included in the present study. We

https://doi.org/10.5194/egusphere-2025-3630
Preprint. Discussion started: 10 October 2025

display sample data collected from September 1 to May 30 from the SMAP pixels centred at 51.64°N, 106.62°W (SK1) and 51.64°N, 106.24°W (SK3) for 2017-18 and 2015-16, respectively, in Figures 2 and 4. These pixels, SK1 and SK3 feature the most complete suite of measurements captured by the KSMN, in particular air temperature at 2 m, as well as soil temperature at 2.5 cm and 5 cm.

Following the methods outlined in Section 2.4, Figures 3 and 5 display SurFCs and SurTCs branches where ${T_B}^H$ is plotted against various in situ temperature sources (i.e., air temperature, soil temperature at 2.5 cm depth, soil temperature at 5 cm depth) for SK1 and SK3. For comparison, we have included similar curves derived using NPR plotted against those same temperature sources. Shaded in red, we show the region where a 'thawed' classification is expected based on a 0.15 °C threshold—the gold standard for validation. The region shaded in blue shows where a 'frozen' classification is expected on the NPR or ${{T_B}^H}_{\text{min}}$ thresholds for that pixel. It follows that measurements falling in the purple shaded region, where red and blue shaded regions overlap, are Type I errors—false positives. Measurements in the unshaded region are then Type II errors—false negatives.

The classification threshold based on NPR values leads to a bisection around a value at the abscissa, dividing the NPR-T phase space into quadrants (FP, TN, TP, FN) in conjunction with the "gold standard" test threshold at 0.15 °C. However, by identifying the temperature at which the ${{T_B}^H}_{\text{min}}$ occurs as our observation threshold, we divide the ${T_B}^H$-T phase space into thirds, eliminating one type of error (Type I or II). The remaining error type depends on the observed threshold's relation to the "gold standard" discriminator of 0.15 °C.

The remotely sensed ${T_B}^H$ plotted against in situ temperatures display a structure similar to that of SFCs when using temperature measurements at depths of 2.5 and 5 cm—the latter being the standard depth for soil moisture validation sites and SMAP products. In the case of air temperature measurements, the structure is harder to discern as it is unstable around the freezing/melting temperature; this is most visible on Figure 5a. The data-driven thresholds for surface F/T classification are within 1.5°C of the 0.15 °C "gold standard test" threshold assumed for SMAP validation.

Figures 3d-e and 5d-e show the current SMAP classification and validation results using NPR. There is an increase in Type II errors when validating NPR observations, which is greatest when validating against air temperature and decreases with measurement depth.

https://doi.org/10.5194/egusphere-2025-3630
Preprint. Discussion started: 10 October 2025

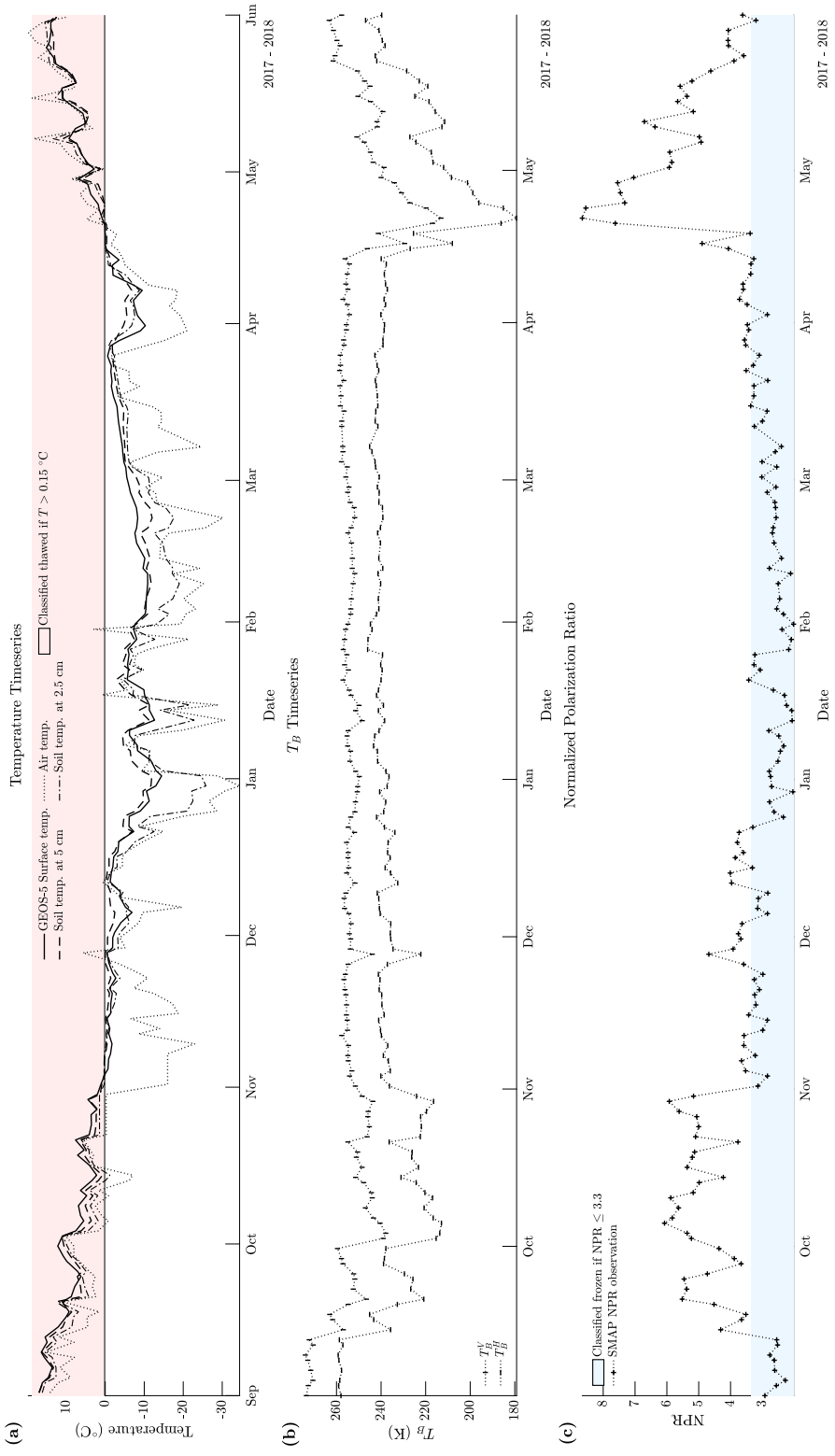

Figure 2. Time series for the SK1 pixel during winter 2017–2018, showing **(a)** in situ air temperature at a height of 1 m and soil temperatures at depths of 2.5 cm and 5 cm, **(b)** T_B in H and V polarizations, and **(c)** NPR. The red shading marks thawed conditions based on the "gold standard" temperature discriminator of 0.15 °C for air and soil temperatures; the blue shading marks frozen conditions. For the NPR algorithm, frozen conditions are based on a threshold of 3.3.

https://doi.org/10.5194/egusphere-2025-3630
Preprint. Discussion started: 10 October 2025

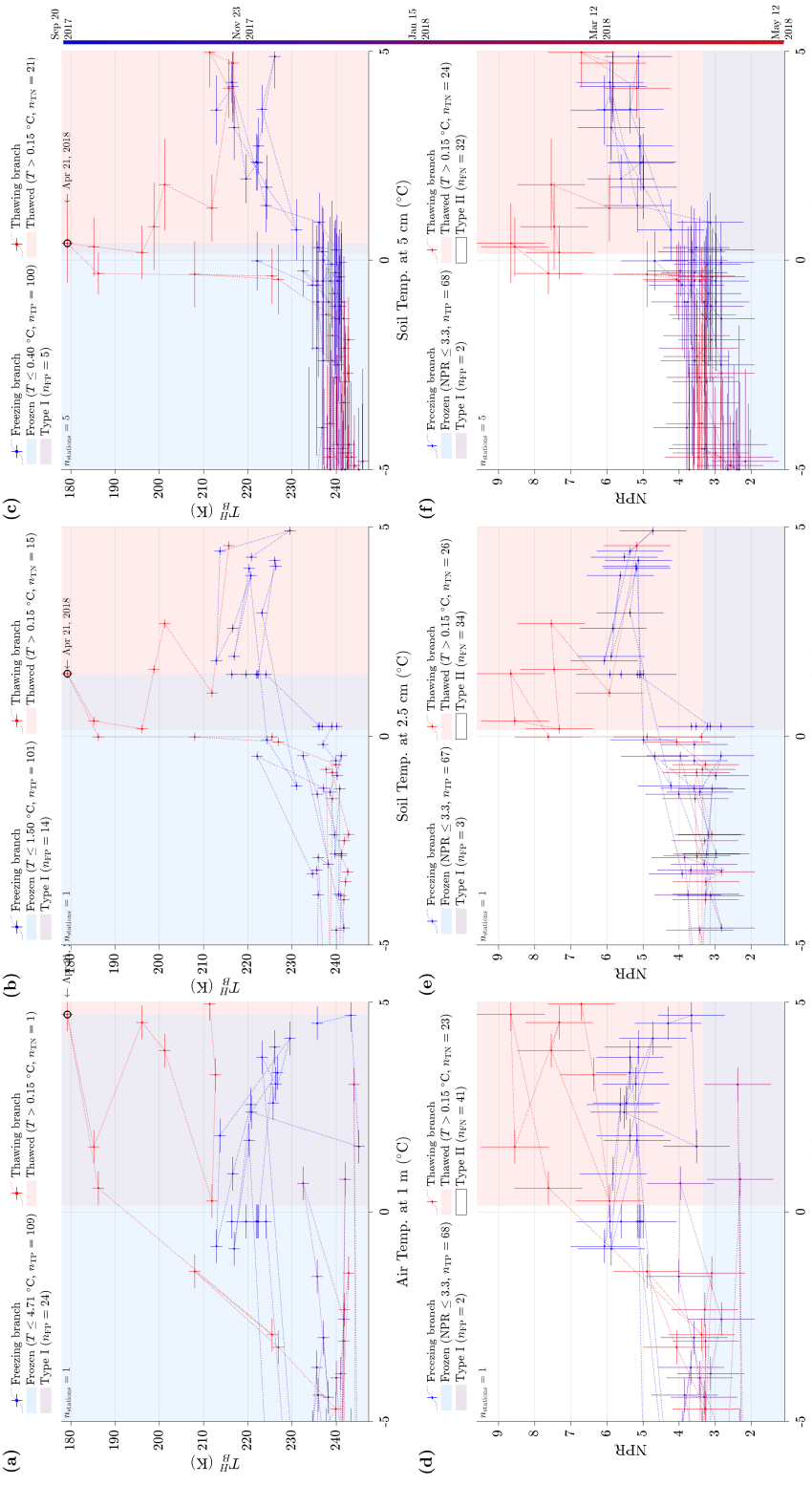

Figure 3. SurFC plots for the SK1 pixel during winter 2017–2018, showing freezing branches in blue and thawing branches (SurTC) in red. Panels **(a–c)** use $T_B{}^H$ measurements; panels **(d–f)** use NPR. Each is plotted against: (a,d) air temperature (n=1), (b,e) soil temperature at 2.5 cm depth (n=1), and (c,f) soil temperature at 5 cm depth (n=5). The red vertical shading marks thawed conditions based on the "gold standard" temperature discriminator of 0.15 °C; the blue vertical shading marks frozen conditions based on $T_B{}^H{}_{\text{min}}$; and the horizontal blue shading marks frozen conditions from the NPR-based discriminator. $T_B{}^H$ observations are temporally connected to highlight the F/T transition. Only data acquired at temperatures ≤ 5 °C were included.

https://doi.org/10.5194/egusphere-2025-3630
Preprint. Discussion started: 10 October 2025

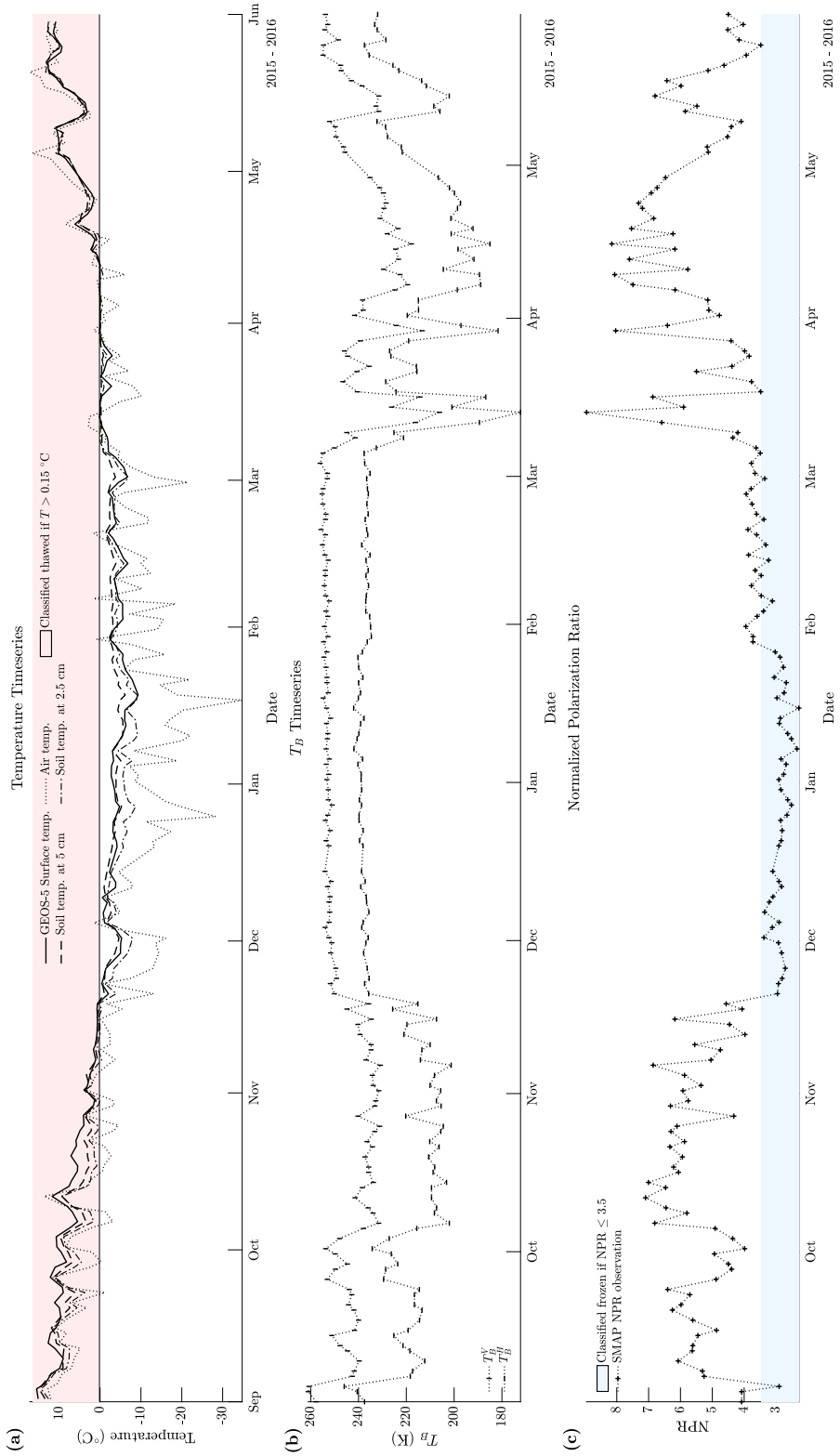

Figure 4. Time series for the SK3 pixel during winter 2015–2016, showing **(a)** in situ air temperature at a height of 1 m and soil temperatures at depths of 2.5 cm and 5 cm, **(b)** T_B in H and V polarizations, and **(c)** NPR. The red shading marks thawed conditions based on the "gold standard" temperature discriminator of 0.15 °C for air and soil temperatures; the blue shading marks frozen conditions. For the NPR algorithm, frozen conditions are based on a threshold of 3.5.

https://doi.org/10.5194/egusphere-2025-3630
Preprint. Discussion started: 10 October 2025

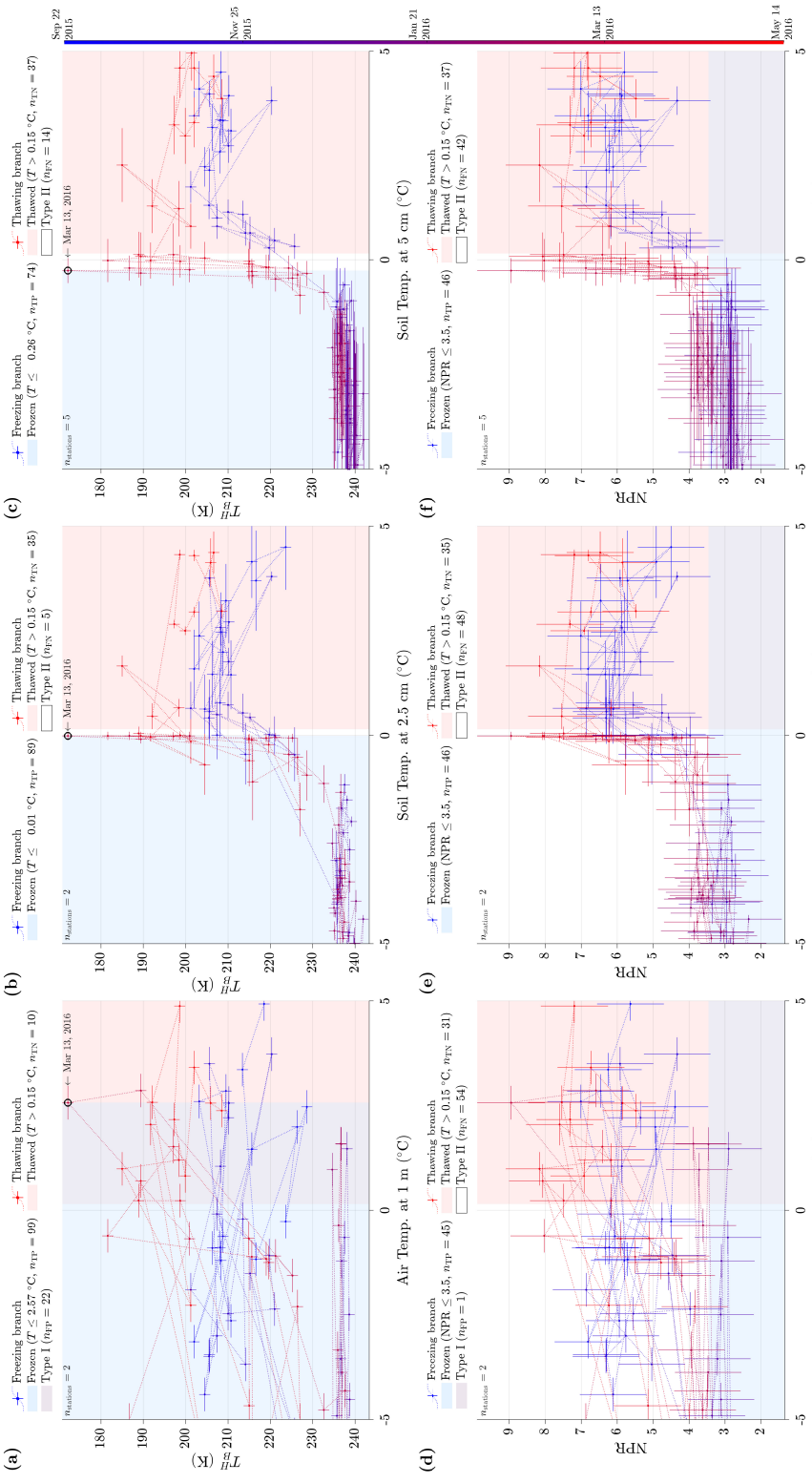

Figure 5. SurFC plots for the SK3 pixel during winter 2015–2016, showing freezing branches in blue and thawing branches (SurTC) in red. Panels **(a–c)** use $T_B{}^H$ measurements; panels **(d–f)** use NPR. Each is plotted against: (a,d) air temperature (n=2), (b,e) soil temperature at 2.5 cm depth (n=2), and (c,f) soil temperature at 5 cm depth (n=5). The red vertical shading marks thawed conditions based on the "gold standard" temperature discriminator of 0.15 °C; the blue vertical shading marks frozen conditions based on $T_B{}^H{}_{\min}$; and the horizontal blue shading marks frozen conditions from the NPR-based discriminator. $T_B{}^H$ observations are temporally connected to highlight the F/T transition. Only data acquired at temperatures $\leq$ 5 °C were included.

https://doi.org/10.5194/egusphere-2025-3630
Preprint. Discussion started: 10 October 2025

3.2 SurFCs and SurTCs from in situ and GEOS-5 FP soil temperature estimates

We extend the methodology to a different geography by using in situ data from the RISMA network stations in Manitoba. This network is instrumented as a core validation site (CVS) which, as a standard, provide soil temperature at a depth of 5 cm. We display the data collected from September 1 to May 30 from the SMAP pixels centred at 49.87 °N, 98.03°W (MB1) and 49.43°N, 98.03°W (MB2) for 2019-20 and 2016-17, respectively, in Figures 6 and 8.

Figures 7 and 9 display SurFCs and SurTCs constructed using in situ soil temperatures and predictions from the GEOS-5 FP product. These pixels, MB1 and MB2, are instrumented for measuring soil temperature and permittivity at a depth of 5 cm. Again, for comparison, we have included similar curves derived using NPR plotted against those same temperature sources. As before, shaded in red we show the region where a 'thawed' classification is expected based on a 0.15 °C threshold. The region shaded in blue shows where a 'frozen' classification is expected on the ${T_B}^H{}_{\min}$ or NPR thresholds for that pixel. Thus, the NPR plots below, Figures 7 (c-d) and 9 (c-d), can also be interpreted as a graphical confusion matrix.

As before, the remotely sensed ${T_B}^H$ plotted against the in situ temperatures display a structure similar to that of SFCs including hysteretic thawing branches STCs. In the case of GEOS-5 FP predictions, the structure is visible, but less clearly. Both data-driven thresholds for surface F/T classification are within ± 0.1 °C of the 0.15 °C threshold assumed for the SMAP validation. On the other hand, the current SMAP classification validated against in situ and the GEOS-5 FP forecast product can be seen in the NPR figures. Again, Figures 8 (b) and 9 (b) display similar structures to the SFCs, including hysteretic thawing branches (STCs).

https://doi.org/10.5194/egusphere-2025-3630
Preprint. Discussion started: 10 October 2025

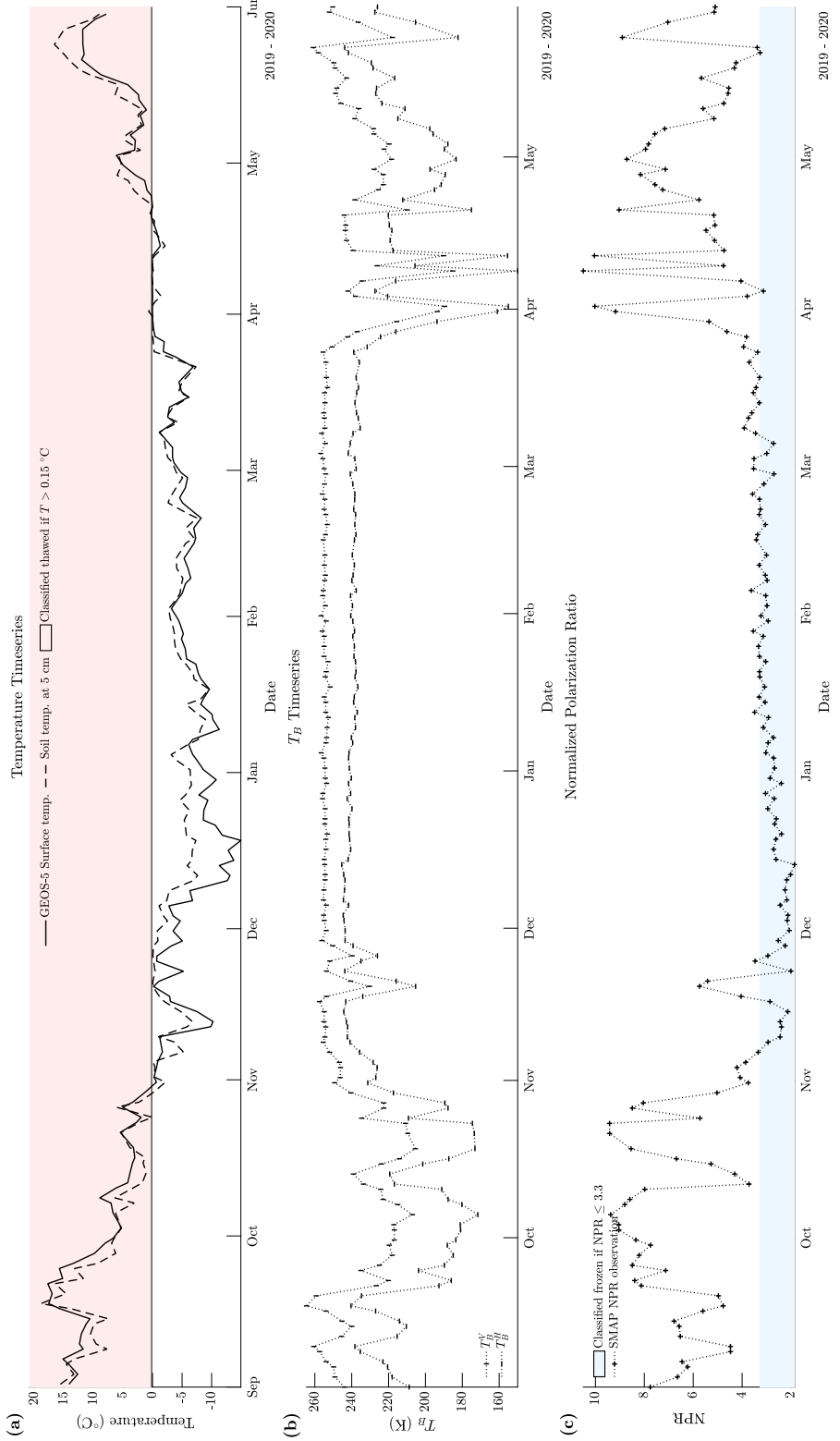

Figure 6. Time series for the MB1 pixel during winter 2019–2020, showing **(a)** in situ soil temperature at a depth of 5 cm and GEOS-5 FP assimilated prediction temperature (mean of 0–10 cm layers), **(b)** T_B in H and V polarizations, and **(c)** NPR. The red shading marks thawed conditions based on the "gold standard" temperature discriminator of 0.15 °C for soil temperatures; the blue shading marks frozen conditions. For the NPR algorithm, frozen conditions are based on a threshold of 3.3.

https://doi.org/10.5194/egusphere-2025-3630
Preprint. Discussion started: 10 October 2025

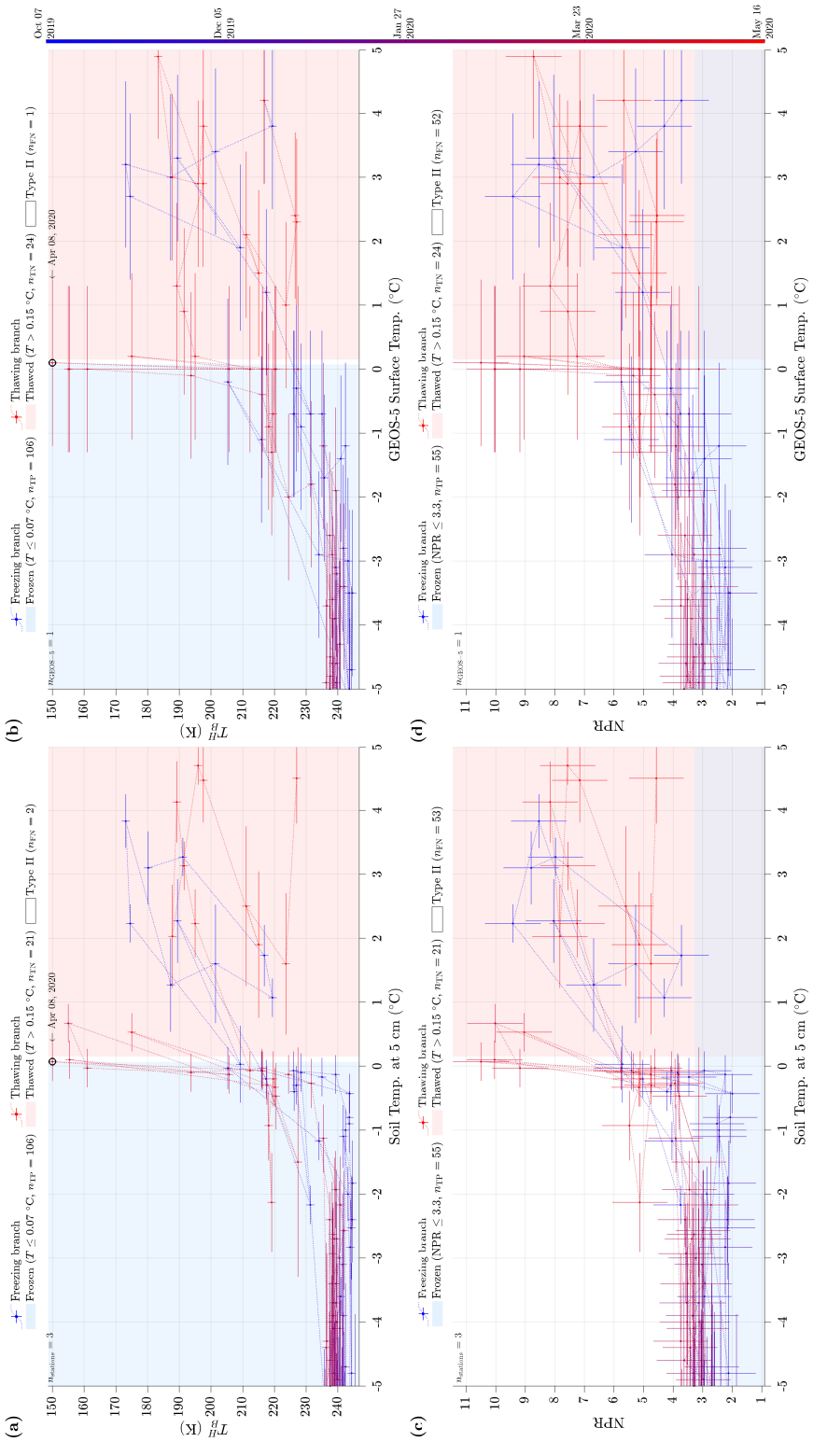

Figure 7. SurFC plots for the MB1 pixel during winter 2019–2020, showing freezing branches in blue and thawing branches (SurTC) in red. Panels **(a–b)** use $T_B{}^H$ measurements; panels **(c–d)** use NPR. Each is plotted against: (a,c) soil temperature at 5 cm depth (n=4), and (b,d) the GEOS-5 FP assimilated prediction temperature (mean of 5–15 cm and 15–35 cm layers). The red vertical shading marks thawed conditions based on the "gold standard" temperature discriminator of 0.15 °C; the blue vertical shading marks frozen conditions based on $T_B{}^H{}_{\min}$; and the horizontal blue shading marks frozen conditions from the NPR-based discriminator. $T_B{}^H$ observations are temporally connected to highlight the F/T transition. Only data acquired at temperatures ≤ 5 °C were included.

https://doi.org/10.5194/egusphere-2025-3630
Preprint. Discussion started: 10 October 2025

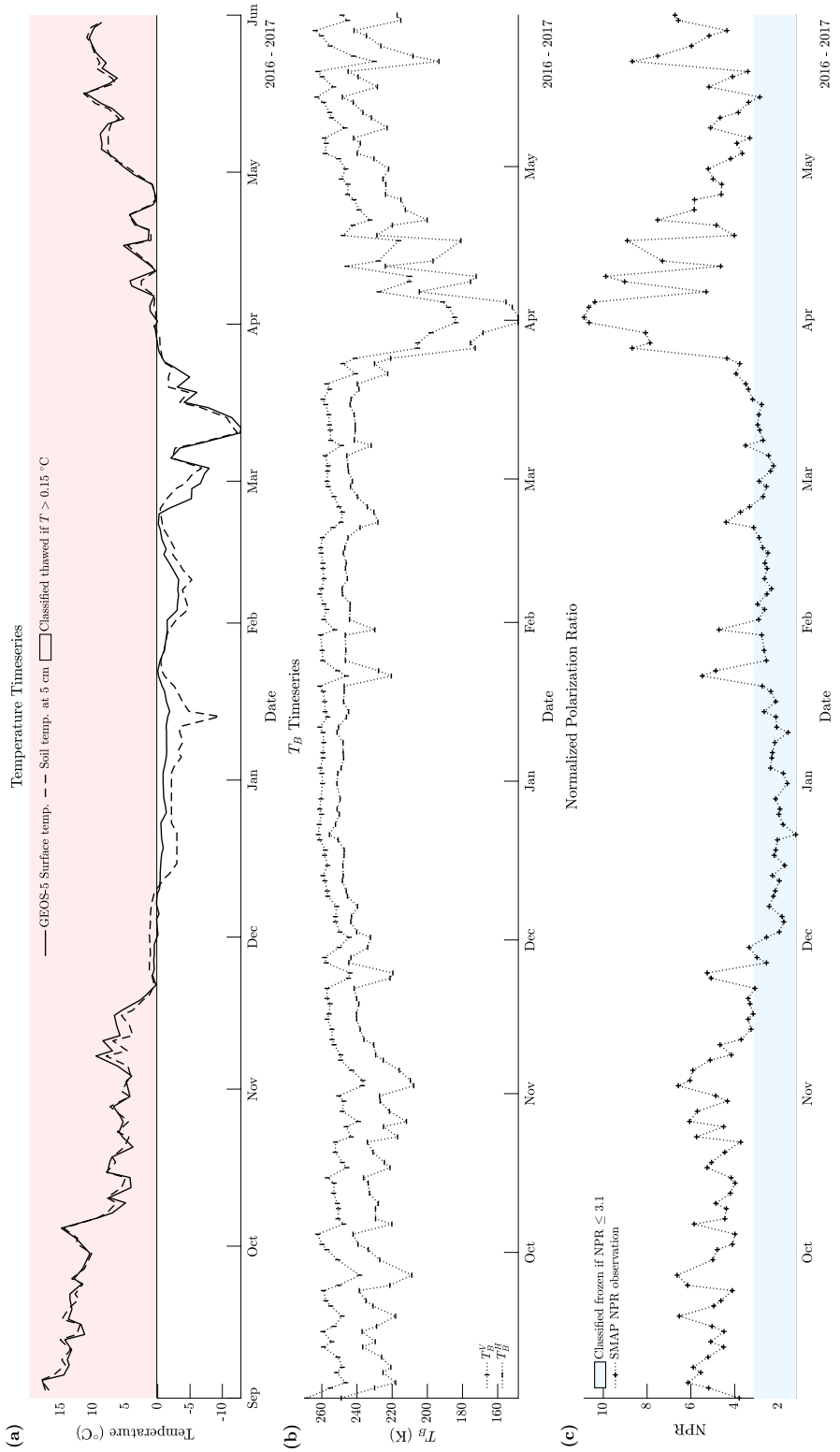

Figure 8. Time series for the MB2 pixel during winter 2016–2017, showing **(a)** in situ soil temperature at a depth of 5 cm and GEOS-5 FP assimilated prediction temperature (mean of 5–15 cm and 15–35 cm layers), **(b)** T_B in H and V polarizations, and **(c)** NPR. The red shading marks thawed conditions based on the "gold standard" temperature discriminator of 0.15 °C for soil temperatures; the blue shading marks frozen conditions. For the NPR algorithm, frozen conditions are based on a threshold of 3.1.

https://doi.org/10.5194/egusphere-2025-3630
Preprint. Discussion started: 10 October 2025

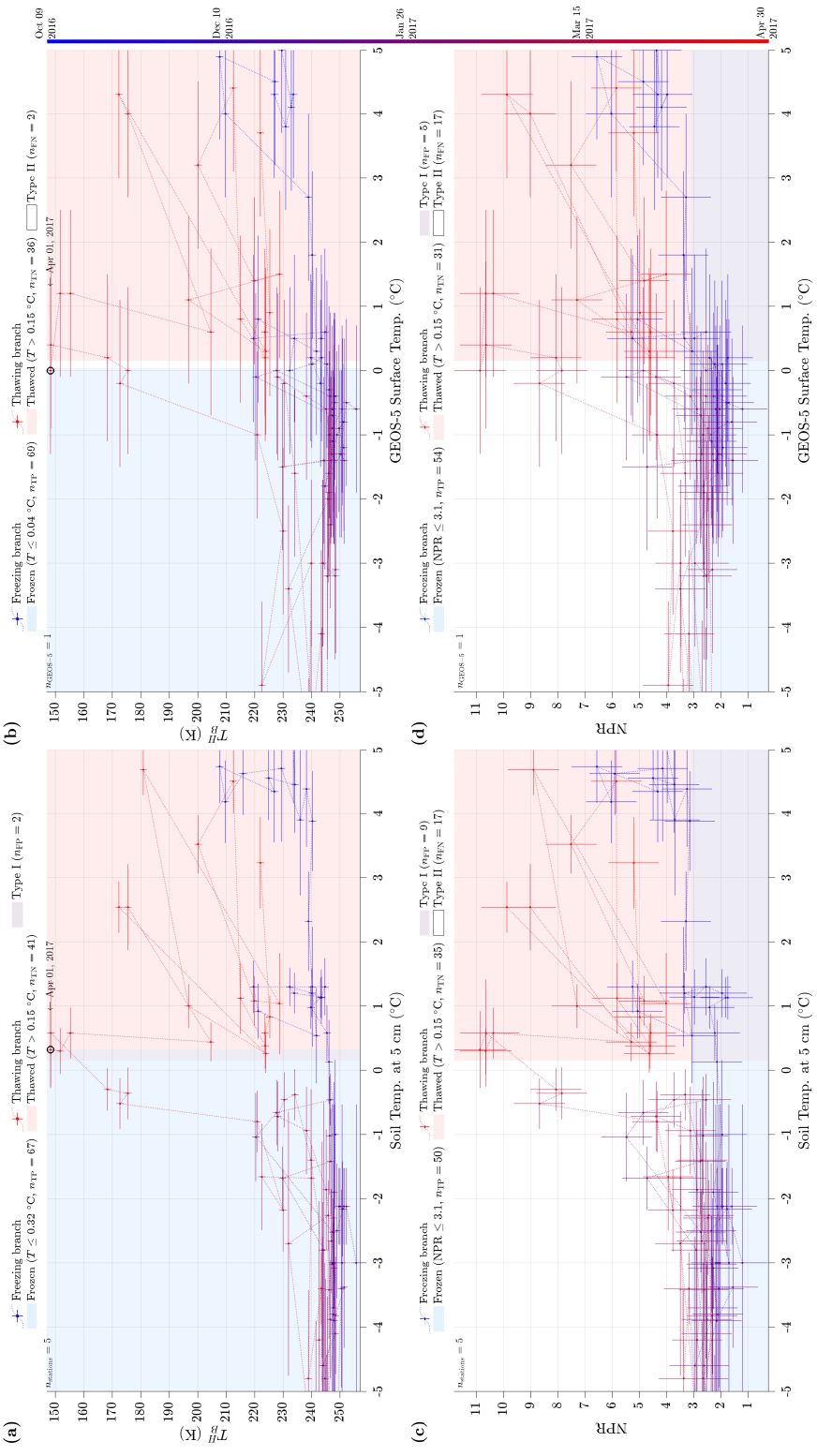

Figure 9. SurFC plots for the MB2 pixel during winter 2016–2017, showing freezing branches in blue and thawing branches (SurTC) in red. Panels **(a–b)** use $T_B{}^H$ measurements; panels **(c–d)** use NPR. Each is plotted against: (a,c) soil temperature at 5 cm depth (n=4), and (b,d) the GEOS-5 FP assimilated prediction temperature (mean of 5–15 cm and 15–35 cm layers). The red vertical shading marks thawed conditions based on the "gold standard" temperature discriminator of 0.15 °C; the blue vertical shading marks frozen conditions based on $T_B{}^H{}_{\text{min}}$; and the horizontal blue shading marks frozen conditions from the NPR-based discriminator. $T_B{}^H$ observations are temporally connected to highlight the F/T transition. Only data acquired at temperatures ≤ 5 °C were included.

https://doi.org/10.5194/egusphere-2025-3630
Preprint. Discussion started: 10 October 2025

3.3 SurTCs for surface F/T classification

The results presented so far show an improvement in the classification accuracy when considering the relationship between ${T_B}^H$ and thermodynamic temperature as opposed to relative changes on the difference of the acquired ${T_B}^H$ and ${T_B}^V$ signatures. Indeed, we created a surface F/T classification product based on ${T_B}^H{}_{\min}$ and GEOS-5 FP forecast surface temperature. This product was compared against the "gold standard" classification product—a 0.15 °C threshold—applied to the available in situ temperature measurements (5 cm in depth in this case). The resulting accuracy, F_1-score, and LR^- statistics are shown below in Figures 10, 11, and 12.

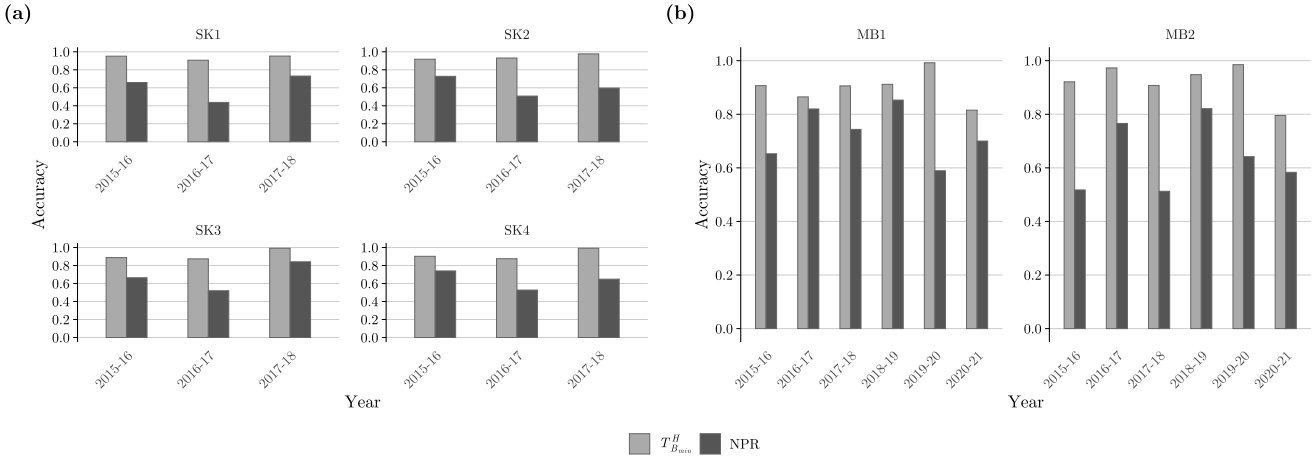

Figure 10. Accuracy for the proposed ${T_B}^H{}_{\min}$ (light grey) and current NPR (dark grey) F/T classification methods, by SMAP pixel and year. Both methods were validated against in situ temperature measurement acquired 5 cm below the surface, which were classified as frozen when the temperature was below 0.15 °C for **(a)** the KSMN in Saskatchewan (SK1-SK4) and **(b)** RISMA Network stations in Manitoba (MB1 and MB2).

Across both Manitoba and Saskatchewan datasets, the ${T_B}^H{}_{\min}$ approach outperformed NPR in detecting freeze/thaw state. For MB, mean accuracy improved from 0.683 to 0.911 (+33.4 %), and mean F1 from 0.746 to 0.944 (+26.5 %). For SK, improvements were larger, with accuracy increasing from 0.633 to 0.930 (+46.9 %) and F1 from 0.644 to 0.947 (+47.0 %). Combined, these gains amounted to a +39.8 % increase in accuracy and +36.0 % in F1.

Across both Manitoba and Saskatchewan datasets, the ${T_B}^H{}_{\min}$ approach consistently outperformed NPR in detecting F/T state. For MB, mean accuracy improved from 0.68 to 0.91 (+33.4 %), and mean F1 from 0.75 to 0.94 (+25 %). For SK, improvements were larger, with accuracy increasing from 0.63 to 0.93 (+47.6 %) and F_1 from 0.64 to 0.95 (+48.4 %). Combined, these gains amounted to a +39.4 % increase in accuracy and +36.2 % in F_1.

Equally notable are the reductions in false-negative rate, captured by LR^-. For MB, LR^- decreased from 0.46 to 0.002 (–99.6 %), effectively eliminating thaw-state omissions. For SK, LR^- fell from 0.52 to 0.09 (–82.7 %), an order-of-magnitude improvement. These gains were accompanied by reduced variability across years and sites: standard deviations in accuracy and

https://doi.org/10.5194/egusphere-2025-3630
Preprint. Discussion started: 10 October 2025

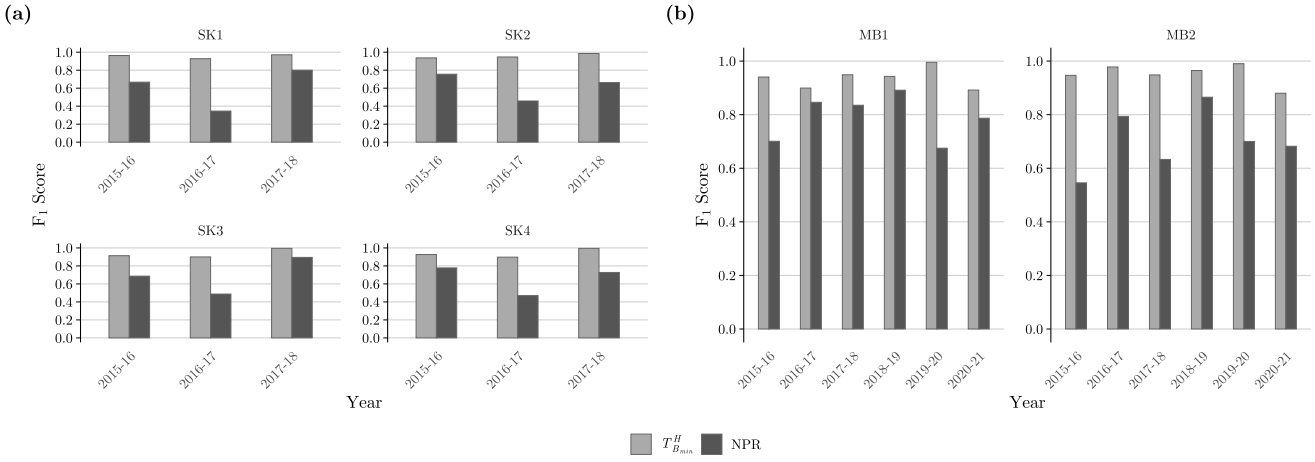

Figure 11. F_1 score for the proposed $T_B{}^H{}_{\text{min}}$ method (light grey) and the current NPR method (dark grey) by SMAP pixel and year. Both methods were validated against in situ soil temperatures at 5 cm depth, classified as frozen when below 0.15 °C: (a) the KSMN in Saskatchewan (SK1–SK4) and (b) the RISMA Network in Manitoba (MB1 and MB2).

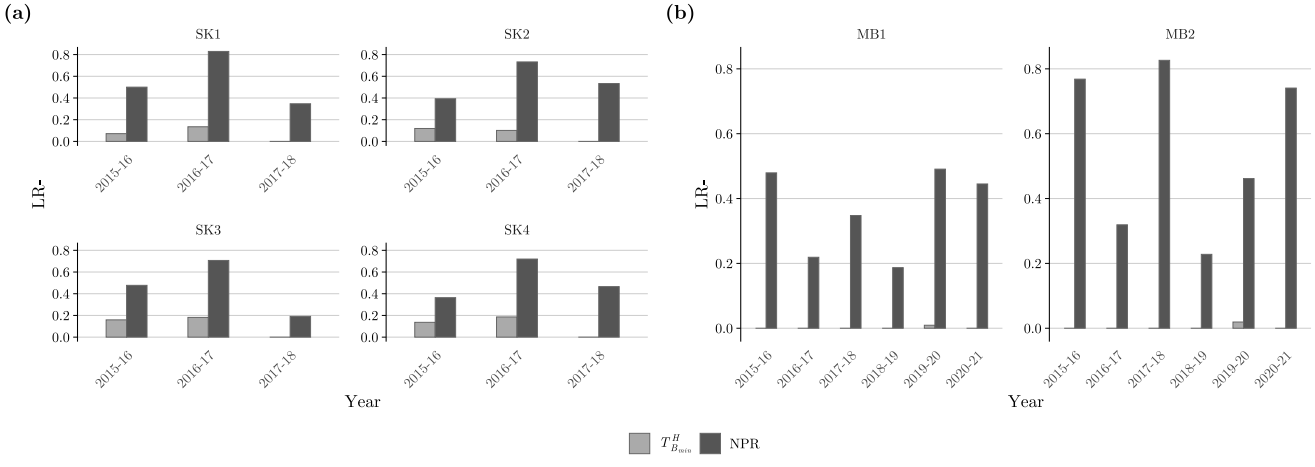

Figure 12. Negative likelihood ratio (LR^-) for the proposed $T_B{}^H{}_{\text{min}}$ method (light grey) and the current NPR method (dark grey) by SMAP pixel and year. Both methods were validated against in situ soil temperatures at 5 cm depth, classified as frozen when below 0.15 °C: (a) the KSMN in Saskatchewan (SK1–SK4) and (b) the RISMA Network in Manitoba (MB1 and MB2).

370 F_1 for $T_B{}^H{}_{\text{min}}$ were roughly half those of NPR, and LR^- variability was reduced by more than an order of magnitude in MB. Together, these results indicate that $T_B{}^H{}_{\text{min}}$ can be more accurate, stable and operationally reliable across diverse mid-latitude agricultural landscapes.

https://doi.org/10.5194/egusphere-2025-3630
Preprint. Discussion started: 10 October 2025

Table 2. Freeze–thaw classification performance for NPR and $T_B{}^H{}_{\min}$ across Manitoba (MB) and Saskatchewan (SK). Values are mean (SD). Changes are relative to NPR.

Dataset	Accuracy		F_1-score		LR^-		Change (%)		
	NPR	$T_B{}^H{}_{\min}$	NPR	$T_B{}^H{}_{\min}$	NPR	$T_B{}^H{}_{\min}$	Accuracy	F_1	LR^-
MB	0.68 (0.12)	0.91 (0.06)	0.75 (0.11)	0.94 (0.04)	0.46 (0.22)	0.002 (0.006)	+33.8	+25.3	−99.6
SK	0.63 (0.12)	0.93 (0.04)	0.64 (0.17)	0.95 (0.04)	0.52 (0.19)	0.09 (0.07)	+47.6	+48.4	−82.7
Combined	0.66 (0.12)	0.92 (0.05)	0.69 (0.15)	0.94 (0.04)	0.49 (0.20)	0.05 (0.07)	+39.4	+36.2	−89.8

Notes. NPR: normalized polarization ratio (SMAP baseline). $T_B{}^H{}_{\min}$: threshold derived from the minimum horizontally polarized brightness temperature.

LR^-: negative likelihood ratio (FN rate / TN rate).

3.3.1 Classification under-performance in winter 2020-21

There was one year in which the proposed $T_B{}^H{}_{\min}$ classification relatively underperformed compared to other years, and approached the minimum accuracy threshold of 80%. This occurred at pixels MB1 and MB2 during the 2020-21 winter. To understand this change in behaviour, time series complemented with GlobSnow SWE and network rainfall measurements as well SurFCs of the corresponding scene are found on Figures 13, and 14.

SurFCs derived from the MB1 pixel $T_B{}^H$ (a-b) and NPR (c-d) in the winter of 2020-2021. The $T_B{}^H$ and NPR are plotted against soil temperature at a depth of 5 cm (a, c; n=4) and the GEOS-5 FP assimilated prediction temperature (mean of 0 and 10 cm layers) for the pixel surface (b, d). The 0.15 °C threshold for soil temperatures—the gold standard classifier—is shown in the vertical red shading. The classifier based on the temperature at the minimum $T_B{}^H$ is shown as the vertical blue shading. Lastly, the NPR based classifier is shown as the horizontal blue shading. Thus, the blue shading shows the observations classified as frozen using both techniques and the red shading shows the gold standard classification (0.15 °C). Note the $T_B{}^H$ observations are connected temporally to highlight the time evolution seen in the thaw process

The scene reached a minimum $T_B{}^H$ at 167.8 K on May 22, 2021, while the soil temperature was at 9.0 °C, which is outside of the ± 5 °C search window for scoping relevant phenomena. Within that window, we see a $T_B{}^H{}_{\min}$ reaches a value of 214.1 K at a, relatively warm, thermodynamic temperature of 4.1 °C on May 3, 2021 - 18 days after the last 0 °C reading. With the complementing rainfall data from the network, it is notable that these spikes in $T_B{}^H$ are associated with heavy precipitation events. On May 2, there was a rainfall event totalling 4.2 ± 1.5 mm. From May 19 to May 22 a total of 42 ± 21 mm of rain fell with 37 ± 21 mm falling on the last day.

Soil temperature measurements reach temperatures above 0 °C for the first time that year on March 21, 2021, with a fluctuation around that value from March 21 until May 1, 2021. We interpret this time frame as a the zero-curtain period. during which $T_B{}^H{}_{\min}$ reaches a value of 229.0 K at on April 22, 2021 at a thermodynamic temperature of 1.6 °C. This is consistent with the GlobSnow estimate for the snowpack, which goes to 0 mm on April 26, 2021.

https://doi.org/10.5194/egusphere-2025-3630
Preprint. Discussion started: 10 October 2025

The only visible peaks around the 0.15 °C transition temperature belong to the SurFC freezing branch, with a ${T_B}^H{}_{\text{min}}$ value of 218.3 K on October 31, 2020 at a thermodynamic temperature of 1.0 °C and ${T_B}^H{}_{\text{min}}$ value of 218.6 K on December 10, 2020 at a thermodynamic temperature of 0 °C. These results are indicative of a relative reduction in the snowpack during the seasonal thaw, compared to other years.

Indeed, one of the top weather stories for 2021 was an extraordinary drought with widespread, severe and long lasting dryness. According to ECCC, “the seeds of this drought were sown months, if not seasons, before 2021. Across much of the west, fields through winter 2020-21 were brown for more days than they were white with snow. Southern Manitoba was Canada’s epicentre for drought, especially in the Red River Valley and the Interlake region. Winnipeg had its two driest back-to-back years in over a century." These two regions abut our study area. As well, according Manitoba’s Department of Environment and Climate Change Drought Monitor for May 2021 reported well below normal winter precipitation, which resulted in insufficient spring runoff. In the context of the proposed ${T_B}^H{}_{\text{min}}$ classification, it shows one of the limitations of the method is that in years with a very reduced snowpack, heavy rainfall events may be confounded with transition thresholds.

https://doi.org/10.5194/egusphere-2025-3630
Preprint. Discussion started: 10 October 2025

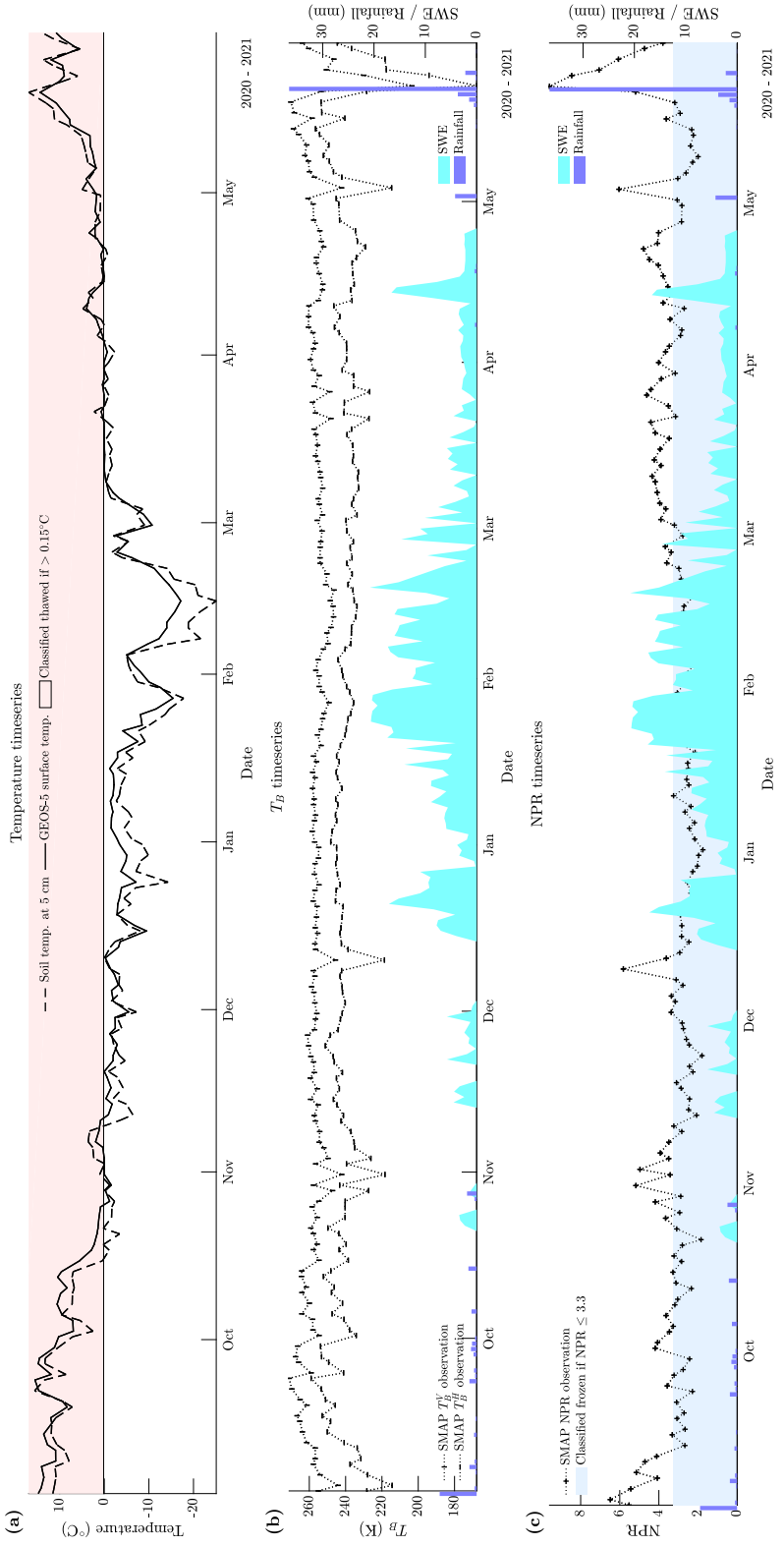

Figure 13. Time series for the MB1 pixel during winter 2020–2021, showing **(a)** in situ soil temperature at a depth of 5 cm and GEOS-5 FP assimilated prediction temperature (mean of 5–15 cm and 15–35 cm layers), **(b)** T_B in H and V polarizations, and **(c)** NPR. The red shading marks thawed conditions based on the "gold standard" temperature discriminator of 0.15 °C for soil temperatures; the blue shading marks frozen conditions. For the NPR algorithm, frozen conditions are based on a threshold of 3.3. **(b)** and **(c)** also include precipitation data from the weather station (blue) and snow water equivalent (SWE) from the GlobSnow product (cyan).

https://doi.org/10.5194/egusphere-2025-3630
Preprint. Discussion started: 10 October 2025

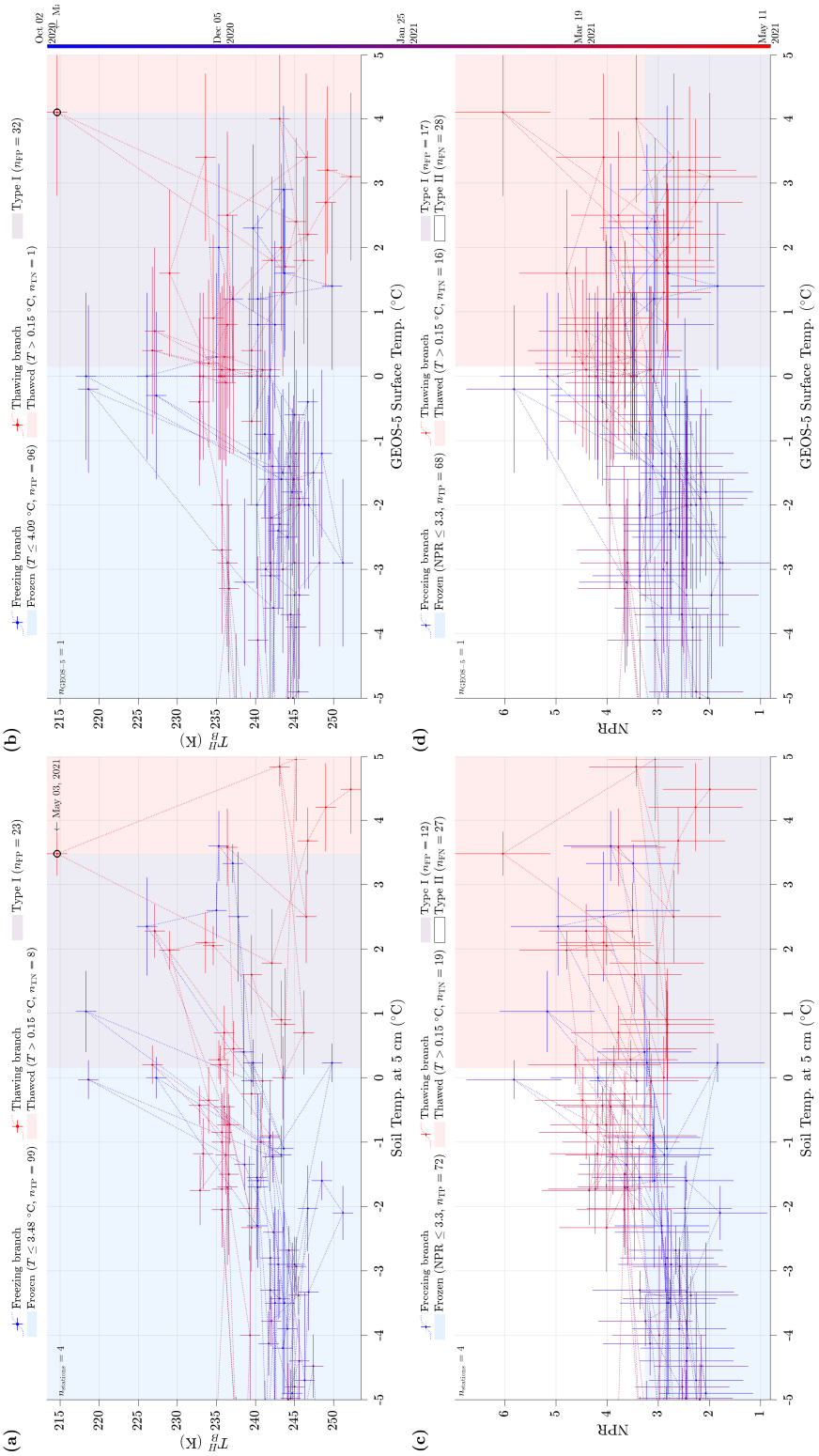

Figure 14. SurFC plots for the MB1 pixel during winter 2020–2021, showing freezing branches in blue and thawing branches (SurTC) in red. Panels **(a–b)** use $T_B{}^H$ measurements; panels **(c–d)** use NPR. Each is plotted against: (a,c) soil temperature at 5 cm depth (n=4), and (b,d) the GEOS-5 FP assimilated prediction temperature (mean of 5–15 cm and 15–35 cm layers). The red vertical shading marks thawed conditions based on the "gold standard" temperature discriminator of 0.15 °C; the blue vertical shading marks frozen conditions based on $T_B{}^H{}_{\min}$; and the horizontal blue shading marks frozen conditions from the NPR-based discriminator. $T_B{}^H$ observations are temporally connected to highlight the F/T transition. Only data acquired at temperatures $\leq$ 5 °C were included.

https://doi.org/10.5194/egusphere-2025-3630
Preprint. Discussion started: 10 October 2025

4 Discussion

In Sections 3.1 and 3.2, our results show that (1) remotely sensed T_B and in situ soil temperature can be used to produce SurFCs and SurTCs (SFCs and STCs at the satellite scale). In Section 3.2, we show (2) remotely sensed T_B and modelled thermodynamic temperature can be used to produce SurFCs and SurTCs at the satellite scale. In Section 3.3, we demonstrate how (3) these SurTCs can be used to identify an extrinsic data-driven threshold for soil moisture F/T state classification. Lastly, in Section 3.3 we present how (4) SurTCs can serve as a tool for surface F/T classification in a remote sensing context, and we also explored their limitations. Current detection and validation methodologies can be improved by taking these findings into consideration.

4.1 Similarities and differences between SFCs and SurFCs

Our results confirm that plotting satellite brightness temperature against surface temperature produces curves analogous to SFCs. The key features that define an SFC—namely, (i) the initial water content at full thaw, (ii) the bulk freezing/melting point, and (iii) the residual (unfreezable) water content at low temperatures—can also be identified in the satellite-derived SurFC curves. In particular, the distinct dip in ${T_B}^H$ as the landscape transitions from frozen to thawed (or vice versa) is qualitatively similar to the drop in unfrozen water content in an SFC curve (Élise Devoie et al., 2022).

One important difference between laboratory-measured SFCs and our satellite SurFCs is the origin of the water contributing to the signal. In controlled soil experiments, changes in unfrozen water content are due solely to soil moisture freezing or thawing. In contrast, our SurFC curves at the landscape scale often capture the influence of snowmelt in addition to soil water. When spring arrives, a surge of liquid water at the surface can come from melting snowpack; this increase in liquid water strongly affects ${T_B}^H$ even if the soil beneath is still partially frozen. Thus, the satellite SurFC is best interpreted as a combined freeze–thaw curve for the soil–snow system in that pixel. Despite this difference, the overall hysteretic pattern (with distinct freezing and thawing branches) is evident in ${T_B}^H$–temperature space, especially when using near-surface soil temperatures (e.g., at 5 cm depth) as the thermodynamic reference.

As seen in our time series and SurFC figures , i.e., Figures 2-9, these transition events occur at ${T_B}^H$ minima (and NPR maxima). We based our analysis on SMAP ${T_B}^H$ because it showed the largest dynamic range in response to F/T transitions and is known to be more sensitive to snow (Leduc-Leballeur et al., 2017; Rautiainen et al., 2014). ${T_B}^H$ drops as the landscape warms and wets, capturing the melting water. On the other hand, NPR combines information from both polarizations as an index and introduces additional uncertainty. In contrast to NPR, ${T_B}^H$ provides a cleaner, absolute signal more directly linked to liquid H_2O. The resemblance of ${T_B}^H$–temperature curves to traditional SFCs, especially around the critical 0.15 °C region, suggests that we can leverage this behaviour to define a data-driven F/T threshold that is tied to actual phase-change dynamics rather than a predefined constant.

https://doi.org/10.5194/egusphere-2025-3630
Preprint. Discussion started: 10 October 2025

4.2 The case against intrinsic thresholds for F/T classification

Classification of the surface F/T essentially asks whether H_2O in the landscape has undergone a phase change (liquid ↔ solid). Physically, freezing and thawing are non-linear first-order transition, defined by the associated latent heat and abrupt changes in entropy. These discontinuities within an evolution are generally marked by critical points in and the notion of complexity is at the heart of the subject (Brunet, 1967). However, applying a threshold-based approach requires correctly identifying the relevant threshold for the system of interest. A key distinction in threshold types is whether they are intrinsic or extrinsic to the system's driving forces.

Many existing satellite F/T classification algorithms rely on intrinsic thresholds. These thresholds are derived from a single observable (or sensor) that indicates a change without direct reference to external conditions. Examples include fixed cutoffs on indices like NPR and on T_B such as the FT-SCV or DAV methods, which look for anomalies or variance changes in the microwave measurements themselves (Rautiainen et al., 2016; Kim et al., 2019; Lv et al., 2022). Intrinsic thresholds are adept at detecting shifts within the observation domain (e.g., a sudden drop in T_B or spike in NPR), but they do not explicitly link those shifts to the environmental driver, that is, the cooling or warming that causes the freezing or thawing.

In contrast, an extrinsic threshold takes the external forcing into account, typically as air or soil temperature, when determining the F/T state. Following Brunet's framework (Brunet, 1967), soil moisture F/T transitions are best characterized as extrinsic, oscillatory change-of-state phenomena. "Extrinsic" in this context means that the transition is controlled by an outside variable (temperature) that gradually pushes the system to a tipping point. In the case of soil F/T, the soil cools or warms under the influence of air temperature until a phase change is triggered in the soil water. By plotting ${T_B}^H$ against temperature and identifying where the thawing curve turns, we tie the classification directly to the physical driver of thaw (heat input) and the system's response (radiometric change). Our findings support the use of these extrinsic thresholds.

In practical terms, this means moving beyond single-sensor logic. Techniques that rely solely on microwave observations risk misidentifying the F/T state when the microwave signal is confounded by factors like dry mineral soil or sensing depth issues. By incorporating a coincident temperature measurement, whether from in situ sensors or a model, we anchor the microwave signal to real thermodynamic conditions. This two-variable approach (microwave T_B plus temperature) transforms the classification problem from a binary yes/no test into analyzing a curve or relationship, which provides more nuance. In essence, extrinsic thresholds offer a more physics-based and robust criterion for F/T discrimination, as they require consistency between what we observe (the radiometric signal) and what we expect from the environment (the presence of freezing or thawing temperatures).

4.3 The case against using air temperature as the extrinsic reference

If extrinsic thresholds are the goal, we must choose an appropriate temperature variable as the reference. A straightforward candidate is air temperature, since it is an external driver of surface F/T and is widely measured. In fact, some current F/T products use air temperature in this way (Kim et al., 2017). However, our analysis reveals significant limitations in using 1 m air temperature to determine the surface F/T state.

https://doi.org/10.5194/egusphere-2025-3630
Preprint. Discussion started: 10 October 2025

Air temperature does not necessarily reflect the actual thermal state of the soil surface, especially under conditions like snow cover. Snow acts as an insulator, creating a thermal lag between the air above and the soil beneath. A sunny day might push air temperature above freezing even while the soil remains frozen, or vice versa at night. In general, factors such as thermal buffering, vertical decoupling, and small-scale heterogeneity can cause the soil's F/T status to deviate from what air temperature alone would suggest (Williamson et al., 2018; Rowlandson et al., 2018; Lv et al., 2022). In our data, plotting ${T_B}^H$ against air temperature yielded a much more scattered and less interpretable curve than using soil temperature. The expected hysteresis (separate freezing and thawing branches) was equivocal when air temperature was the reference, particularly in snow-affected sites (see Figure 5a for example). This led to ambiguity in classification: there were instances where the microwave signal (NPR) indicated a frozen condition, yet the air temperature hovered just above 0 °C, creating a false impression of thaw if air temperature alone were used as the criterion. These kinds of mismatches manifest as increased Type II errors (missed detections of freeze) when air temperature is used for validation.

By contrast, using soil temperature (particularly at a shallow depth like 2.5 or 5 cm) as the extrinsic variable provided a much clearer indication of the phase state of the surface water. In our study, ${T_B}^H$ plotted against in situ soil temperature produced well-formed SurFCs/SurTCs with clear inflection points. Even the GEOS-5 FP modelled soil temperature, while not perfect, yielded a discernible characteristic curve that aligned with the in situ measurements (Figures 7–9). We, therefore, conclude that near-surface soil temperature is a superior extrinsic reference for F/T classification in these environments. After an initial comparison (Section 3.1) demonstrated air temperature's limitations, we omitted air temperature from further threshold analysis and focused on soil-based temperature data (either in situ or model-derived). This choice improved the consistency and physical interpretability of the F/T classification, especially in seasons or locations with snow involvement.

4.4 The case for data-driven surface F/T extrinsic thresholds

Our results show that a classification threshold derived from the ${T_B}^H{}_{\min}$ method outperforms the standard NPR-based approach for detecting F/T state. Across two mid-latitude agricultural regions, the ${T_B}^H{}_{\min}$ method improved mean classification accuracy by 39% (increasing from 66% to 92%) and mean F_1-score by 36%, relative to the baseline NPR method. Equally important, the method dramatically reduced the false-negative rate. The negative likelihood ratio (NLR) dropped by roughly an order of magnitude (82–99% reduction) compared to NPR. The ${T_B}^H{}_{\min}$ approach also proved more stable across years and sites. Interannual and inter-site variability in accuracy and F_1 were about half that of NPR.

This improved consistency reinforces a key point: surface freeze/thaw thresholds should not be universally fixed at 0.15 °C (the traditionally assumed value for validation) without a physical basis. In our study, for instance, air temperature, soil temperature, and radiometric signals each couple to the actual phase-change process in different ways, and each is subject to influences like soil thermal buffering, freezing-point depression in situ, and local heterogeneity. By empirically deriving the threshold from the system's own response (the SurTC), the ${T_B}^H{}_{\min}$ method avoids reliance on an arbitrary cutoff. It thus mitigates location-specific biases and adapts to local conditions, providing a more robust basis for large-scale freeze–thaw monitoring where environmental conditions can vary widely.

https://doi.org/10.5194/egusphere-2025-3630
Preprint. Discussion started: 10 October 2025

5 Conclusions

This study demonstrates that extrinsic thresholds—derived from paired measurements of environmental forcing (soil temperature) and system response ($T_B{}^H$)—provide an operationally viable, physics-based framework for surface F/T classification. While intrinsic thresholds (e.g., the "gold standard" 0.15 °C rule or fixed NPR values) rely on sensor-specific behaviour, extrinsic thresholds are causally anchored in real-world environmental dynamics, improving both accuracy and interpretability.

Our SurFC framework formalizes this dual-measurement strategy, revealing consistent and physically meaningful F/T transitions even under confounding conditions such as melt events or transitional thaw phases. By linking remotely sensed L-band T_B with thermodynamic temperature—, sourced from in situ observations or forecast estimates from GEOS-5 FP—, we demonstrate that satellite-scale F/T detection can be redefined around data-driven, extrinsic thresholds rather than intrinsic, single sensor-derived metrics.

In this study we show that (1) remotely sensed T_B and in situ soil temperature can be used to produce SurFCs—a novel remote sensing analogue to lab-based SFCs. These curves effectively capture transition dynamics at the satellite footprint scale. (2) Forecast-based temperature from GEOS-5 FP can substitute in situ temperature, making the method viable for near-real-time applications. (3) SurTCs can be used to empirically identify extrinsic thresholds, defined at $T_B{}^H{}_{\text{min}}$ relative to soil temperature. This minimizes reliance on somewhat arbitrary cutoffs (e.g., 0.15 °C) and anchors classification in observable environmental interactions. (4) SurFCs serve as a powerful interpretive and classification tool, offering more transparency into the F/T process and supporting validation of existing F/T products.

More generally, we found that NPR-based classification methods, which rely on internal signal variability, are poorly suited for snow-influenced hydrologies where snowmelt dominated the L-band signature. Because they depend solely on internal variability, such methods struggle with these highly dynamic transitions governed by external forcing. Algorithms based only on $T_B{}^P$ variation attempt to identify a surface transition without referencing its environmental cause. As a result, they contain little physical information about the process itself.

By contrast, the SurFC framework introduces a temperature dimension to F/T detection, grounding classification in environmental cause rather than relative signal changes. This requires rejecting the default assumption that 0.15 °C is the universal F/T threshold. Instead, we argue that the F/T threshold should emerge from empirical data, in our case we identified that the temperature at which $T_B{}^H{}_{\text{min}}$ occurs can help identify an actual transition in surface state. This approach improves interpretability and enables better control over classification errors by anchoring transitions in measurable physical phenomena.

Our classification method, based on identifying the thermodynamic temperature corresponding to $T_B{}^H{}_{\text{min}}$, outperformed the NPR method against a 0 °C reference benchmark in all years and metrics analyzed (i.e., Accuracy, F_1-score, LR^-). However, during the 2020–21 winter at MB1 and MB2, which had low snowpack, classification performance dropped below 80%. Ancillary data (GlobSnow SWE, KSMN rainfall, and drought monitor reports) confirm that this dip was likely due to reduced winter snowpack followed by significant rain events, which confounded the $T_B{}^H{}_{\text{min}}$ classification algorithm.

This work strengthens the case for scalable, data-driven approaches to F/T monitoring. By anchoring surface state classification in extrinsic thresholds, it advances a framework that is more responsive to environmental complexity and suitable

https://doi.org/10.5194/egusphere-2025-3630
Preprint. Discussion started: 10 October 2025

for integration into operational remote sensing workflows. As a result, these findings support both improved scientific understanding and more realistic input data for downstream applications, such as cryospheric modelling, water balance studies, and agricultural or land-use decision tools.

Future research should (1) extend the method to finer spatial resolutions (e.g., SMAP Enhanced product or airborne L-band data); (2) investigate the use of SurFCs to disambiguate F/T transitions from dry-down or desiccation; and (3) explore applications in water resource forecasting, climate adaptation, and cold-region hydrology, where accurate phase-state classification has direct policy relevance.

Data availability. An archived dataset containing Kenaston Soil Moisture Network (KSMN) observations, including additional soil property measurements, is available from the Federated Research Data Repository (FRDR), doi:10.20383/101.0200 The Real-Time In-Situ Soil Monitoring for Agriculture (RISMA) dataset is available from Agriculture and Agri-Food Canada via the Agriculture Data Portal (https://agrifood.aquaticinformatics.net/Data/Export) and is maintained as a continuously updated operational dataset without a persistent DOI. The SMAP freeze/thaw product is available from NASA NSIDC: Xu et al. (2023), doi:10.5067/LQQ5I3QVGFTU. The SMAP soil moisture product is available from NASA NSIDC: ONeill et al. (2023), doi:10.5067/K7Y2D8QQVZ4L. The GlobSnow snow water equivalent product is described by Takala et al. (2011), doi:10.1016/j.rse.2011.08.014, and is available from the Finnish Meteorological Institute (https://www.globsnow.info/index.php?page=Data). All metrics used in this study are provided in the Appendix.

https://doi.org/10.5194/egusphere-2025-3630
Preprint. Discussion started: 10 October 2025

Table A1: Classification results and summary statistics by network, pixel, year, predictor, and reference response. Values are counts and metrics per row.

Network	Pixel	Year	Predictor	Reference	P	N	True pos.	True neg.	False pos.	False neg.	Accuracy	F_1-score	LR^-
RISMA	1	2015–16	${T_B}^H{}_{\min}$	$T_{\text{Soil 5 cm}}$	87	31	87	20	11	0	0.907	0.941	0.000
RISMA	1	2015–16	NPR	$T_{\text{Soil 5 cm}}$	87	31	48	29	2	39	0.653	0.701	0.467
RISMA	2	2015–16	${T_B}^H{}_{\min}$	$T_{\text{Soil 5 cm}}$	80	34	80	25	9	0	0.921	0.947	0.000
RISMA	2	2015–16	NPR	$T_{\text{Soil 5 cm}}$	80	34	33	26	8	47	0.518	0.545	0.730
RISMA	1	2016–17	${T_B}^H{}_{\min}$	$T_{\text{Soil 5 cm}}$	67	44	67	29	15	0	0.865	0.899	0.000
RISMA	1	2016–17	NPR	$T_{\text{Soil 5 cm}}$	67	44	55	36	8	12	0.820	0.846	0.205
RISMA	2	2016–17	${T_B}^H{}_{\min}$	$T_{\text{Soil 5 cm}}$	67	44	67	41	3	0	0.973	0.978	0.000
RISMA	2	2016–17	NPR	$T_{\text{Soil 5 cm}}$	67	44	50	35	9	17	0.766	0.794	0.299
RISMA	1	2017–18	${T_B}^H{}_{\min}$	$T_{\text{Soil 5 cm}}$	102	15	102	4	11	0	0.906	0.949	0.000
RISMA	1	2017–18	NPR	$T_{\text{Soil 5 cm}}$	102	15	76	11	4	26	0.744	0.835	0.268
RISMA	2	2017–18	${T_B}^H{}_{\min}$	$T_{\text{Soil 5 cm}}$	101	18	101	7	11	0	0.908	0.948	0.000
RISMA	2	2017–18	NPR	$T_{\text{Soil 5 cm}}$	101	18	50	11	7	51	0.513	0.633	0.576
RISMA	1	2018–19	${T_B}^H{}_{\min}$	$T_{\text{Soil 5 cm}}$	99	37	99	25	12	0	0.912	0.943	0.000
RISMA	1	2018–19	NPR	$T_{\text{Soil 5 cm}}$	99	37	82	34	3	17	0.853	0.891	0.178
RISMA	2	2018–19	${T_B}^H{}_{\min}$	$T_{\text{Soil 5 cm}}$	96	38	96	31	7	0	0.948	0.965	0.000
RISMA	2	2018–19	NPR	$T_{\text{Soil 5 cm}}$	96	38	77	33	5	19	0.821	0.865	0.211
RISMA	1	2019–20	${T_B}^H{}_{\min}$	$T_{\text{Soil 5 cm}}$	108	21	107	21	0	1	0.992	0.995	0.009
RISMA	1	2019–20	NPR	$T_{\text{Soil 5 cm}}$	108	21	55	21	0	53	0.589	0.675	0.491
RISMA	2	2019–20	${T_B}^H{}_{\min}$	$T_{\text{Soil 5 cm}}$	104	30	102	30	0	2	0.985	0.990	0.019
RISMA	2	2019–20	NPR	$T_{\text{Soil 5 cm}}$	104	30	56	30	0	48	0.642	0.700	0.462
RISMA	1	2020–21	${T_B}^H{}_{\min}$	$T_{\text{Soil 5 cm}}$	99	31	99	7	24	0	0.815	0.892	0.000
RISMA	1	2020–21	NPR	$T_{\text{Soil 5 cm}}$	99	31	72	19	12	27	0.700	0.787	0.318
RISMA	2	2020–21	${T_B}^H{}_{\min}$	$T_{\text{Soil 5 cm}}$	99	33	99	6	27	0	0.795	0.880	0.000
RISMA	2	2020–21	NPR	$T_{\text{Soil 5 cm}}$	99	33	59	18	15	40	0.583	0.682	0.507
KSMN	1	2015–16	${T_B}^H{}_{\min}$	$T_{\text{Air 1 m}}$	91	38	91	3	35	0	0.729	0.839	0.000
KSMN	1	2015–16	${T_B}^H{}_{\min}$	$T_{\text{Soil 2.5 cm}}$	87	36	69	36	0	18	0.854	0.885	0.207
KSMN	1	2015–16	${T_B}^H{}_{\min}$	$T_{\text{Soil 5 cm}}$	84	39	78	39	0	6	0.951	0.963	0.071
KSMN	1	2015–16	NPR	$T_{\text{Air 1 m}}$	91	38	40	36	2	51	0.589	0.602	0.588
KSMN	1	2015–16	NPR	$T_{\text{Soil 2.5 cm}}$	87	36	42	36	0	45	0.634	0.651	0.517
KSMN	1	2015–16	NPR	$T_{\text{Soil 5 cm}}$	84	39	42	39	0	42	0.659	0.667	0.500
KSMN	2	2015–16	${T_B}^H{}_{\min}$	$T_{\text{Soil 5 cm}}$	84	37	74	37	0	10	0.917	0.937	0.119
KSMN	2	2015–16	NPR	$T_{\text{Soil 5 cm}}$	84	37	51	37	0	33	0.727	0.756	0.393
KSMN	3	2015–16	${T_B}^H{}_{\min}$	$T_{\text{Air 1 m}}$	99	32	99	10	22	0	0.832	0.900	0.000
KSMN	3	2015–16	${T_B}^H{}_{\min}$	$T_{\text{Soil 2.5 cm}}$	94	35	89	35	0	5	0.961	0.973	0.053
KSMN	3	2015–16	${T_B}^H{}_{\min}$	$T_{\text{Soil 5 cm}}$	88	37	74	37	0	14	0.888	0.914	0.159
KSMN	3	2015–16	NPR	$T_{\text{Air 1 m}}$	99	32	45	31	1	54	0.580	0.621	0.558
KSMN	3	2015–16	NPR	$T_{\text{Soil 2.5 cm}}$	94	35	46	35	0	48	0.628	0.657	0.511

Continued on next page

https://doi.org/10.5194/egusphere-2025-3630
Preprint. Discussion started: 10 October 2025

Table A1 (continued).

Network	Pixel	Year	Predictor	Reference	P	N	True pos.	True neg.	False pos.	False neg.	Accuracy	F_1-score	LR$^-$
KSMN	3	2015–16	NPR	$T_{\text{Soil 5 cm}}$	88	37	46	37	0	42	0.664	0.687	0.477
KSMN	4	2015–16	${T_B}^H{}_{\text{min}}$	$T_{\text{Soil 5 cm}}$	88	35	76	35	0	12	0.902	0.927	0.136
KSMN	4	2015–16	NPR	$T_{\text{Soil 5 cm}}$	88	35	56	35	0	32	0.740	0.778	0.364
KSMN	1	2016–17	${T_B}^H{}_{\text{min}}$	$T_{\text{Air 1 m}}$	86	27	86	13	14	0	0.876	0.925	0.000
KSMN	1	2016–17	${T_B}^H{}_{\text{min}}$	$T_{\text{Soil 2.5 cm}}$	86	26	86	18	8	0	0.929	0.956	0.000
KSMN	1	2016–17	${T_B}^H{}_{\text{min}}$	$T_{\text{Soil 5 cm}}$	89	39	77	39	0	12	0.906	0.928	0.135
KSMN	1	2016–17	NPR	$T_{\text{Air 1 m}}$	86	27	19	27	0	67	0.407	0.362	0.779
KSMN	1	2016–17	NPR	$T_{\text{Soil 2.5 cm}}$	86	26	19	26	0	67	0.402	0.362	0.779
KSMN	1	2016–17	NPR	$T_{\text{Soil 5 cm}}$	89	39	19	37	2	70	0.438	0.345	0.869
KSMN	2	2016–17	${T_B}^H{}_{\text{min}}$	$T_{\text{Soil 5 cm}}$	89	41	80	41	0	9	0.931	0.947	0.101
KSMN	2	2016–17	NPR	$T_{\text{Soil 5 cm}}$	89	41	27	39	2	62	0.508	0.458	0.748
KSMN	3	2016–17	${T_B}^H{}_{\text{min}}$	$T_{\text{Air 1 m}}$	96	32	96	19	13	0	0.898	0.937	0.000
KSMN	3	2016–17	${T_B}^H{}_{\text{min}}$	$T_{\text{Soil 2.5 cm}}$	87	38	87	29	9	0	0.928	0.951	0.000
KSMN	3	2016–17	${T_B}^H{}_{\text{min}}$	$T_{\text{Soil 5 cm}}$	88	39	72	39	0	16	0.874	0.900	0.182
KSMN	3	2016–17	NPR	$T_{\text{Air 1 m}}$	96	32	31	32	0	65	0.492	0.488	0.677
KSMN	3	2016–17	NPR	$T_{\text{Soil 2.5 cm}}$	87	38	29	36	2	58	0.520	0.492	0.713
KSMN	3	2016–17	NPR	$T_{\text{Soil 5 cm}}$	88	39	29	37	2	59	0.520	0.487	0.717
KSMN	4	2016–17	${T_B}^H{}_{\text{min}}$	$T_{\text{Soil 5 cm}}$	86	43	70	43	0	16	0.876	0.897	0.186
KSMN	4	2016–17	NPR	$T_{\text{Soil 5 cm}}$	86	43	27	41	2	59	0.527	0.470	0.737
KSMN	1	2017–18	${T_B}^H{}_{\text{min}}$	$T_{\text{Air 1 m}}$	109	25	109	1	24	0	0.821	0.901	0.000
KSMN	1	2017–18	${T_B}^H{}_{\text{min}}$	$T_{\text{Soil 2.5 cm}}$	101	29	101	14	15	0	0.885	0.931	0.000
KSMN	1	2017–18	${T_B}^H{}_{\text{min}}$	$T_{\text{Soil 5 cm}}$	100	26	100	20	6	0	0.952	0.971	0.000
KSMN	1	2017–18	NPR	$T_{\text{Air 1 m}}$	109	25	68	23	2	41	0.679	0.760	0.387
KSMN	1	2017–18	NPR	$T_{\text{Soil 2.5 cm}}$	101	29	67	26	3	34	0.715	0.784	0.352
KSMN	1	2017–18	NPR	$T_{\text{Soil 5 cm}}$	100	26	68	24	2	32	0.730	0.800	0.329
KSMN	2	2017–18	${T_B}^H{}_{\text{min}}$	$T_{\text{Soil 5 cm}}$	101	28	101	25	3	0	0.977	0.985	0.000
KSMN	2	2017–18	NPR	$T_{\text{Soil 5 cm}}$	101	28	51	26	2	50	0.597	0.662	0.514
KSMN	3	2017–18	${T_B}^H{}_{\text{min}}$	$T_{\text{Air 1 m}}$	109	25	109	3	22	0	0.836	0.908	0.000
KSMN	3	2017–18	${T_B}^H{}_{\text{min}}$	$T_{\text{Soil 2.5 cm}}$	106	24	106	13	11	0	0.915	0.951	0.000
KSMN	3	2017–18	${T_B}^H{}_{\text{min}}$	$T_{\text{Soil 5 cm}}$	104	22	104	21	1	0	0.992	0.995	0.000
KSMN	3	2017–18	NPR	$T_{\text{Air 1 m}}$	109	25	84	22	3	25	0.791	0.857	0.238
KSMN	3	2017–18	NPR	$T_{\text{Soil 2.5 cm}}$	106	24	86	24	0	20	0.846	0.896	0.189
KSMN	3	2017–18	NPR	$T_{\text{Soil 5 cm}}$	104	22	85	21	1	19	0.841	0.895	0.185
KSMN	4	2017–18	${T_B}^H{}_{\text{min}}$	$T_{\text{Soil 5 cm}}$	102	26	102	25	1	0	0.992	0.995	0.000
KSMN	4	2017–18	NPR	$T_{\text{Soil 5 cm}}$	102	26	60	23	3	42	0.648	0.727	0.432

Notes. NPR = normalized polarization ratio; ${T_B}^H{}_{\text{min}}$ = threshold at the minimum horizontally polarized brightness temperature. Reference responses: $T_{\text{Air 1 m}}$ (1 m air temperature); $T_{\text{Soil 5 cm}}$ (soil temperature at 5 cm depth); $T_{\text{Soil 2.5 cm}}$ (soil temperature at 2.5 cm depth); $T_{\text{HPT 5 cm}}$ (HydraProbe soil temperature at

https://doi.org/10.5194/egusphere-2025-3630
Preprint. Discussion started: 10 October 2025

5 cm depth); $T_{\text{GEOS-5 FP}}$ (GEOS-5 FP effective soil temperature ancillary). P = positives; N = negatives; LR^- = negative likelihood ratio (FN rate / TN rate).

Author contributions. R.P.L: Conceptualization, Methodology, Software, Data Curation, Formal Analysis, Validation, Visualization, Funding Acquisition, Writing – Original Draft, Writing – Review & Editing. A.B.: Supervision, Funding Acquisition, Investigation, Writing – Review & Editing. A.C.: Writing – Review & Editing. E.T.: Data Curation, Writing – Review. J.P.: Data Curation, Writing – Review. J.A.: Writing – Review.

Competing interests. The contact author has declared that none of the authors has any competing interests.

Acknowledgements. In preparing this manuscript for submission, the authors used AI-assisted editing tools to help refine language, improve readability, and ensure clarity for a broad scientific audience. All scientific content, data analysis, and interpretations are entirely the authors' own. AI was not used for generating ideas, performing statistical calculations, or producing figures.

This study was supported by the Natural Sciences Engineering Research Council (NSERC) of Canada, through a PhD scholarship awarded to R.P.L., and the Canadian Space Agency (CSA). We would also like to thank the organizers and attendees of the Soil Moisture Active Passive Validation Experiments Workshop 2024 for illuminating presentations and conversations. Finally, we acknowledge the invaluable assistance of our colleagues Kurt Gottfried and Matthew Friesen.

https://doi.org/10.5194/egusphere-2025-3630
Preprint. Discussion started: 10 October 2025

References

Andersland, O. B. and Ladanyi, B.: An Introduction to Frozen Ground Engineering, in: An Introduction to Frozen Ground Engineering, Springer New York, NY, https://doi.org/10.1007/978-1-4757-2290-1, 1994.

Andersland, O. B., David C, W., and Simon H, D.: Hydraulic Conductivity of Frozen Granular Soils, Journal of Environmental Engineering, 122, 212–216, https://doi.org/10.1061/(ASCE)0733-9372(1996)122:3(212), 1996.

Azmatch, T. F., Sego, D. C., Arenson, L. U., and Biggar, K. W.: Using soil freezing characteristic curve to estimate the hydraulic conductivity function of partially frozen soils, Cold Regions Science and Technology, 83-84, 103–109, https://doi.org/10.1016/j.coldregions.2012.07.002, 2012.

Barry, R. G. and Gan, T. Y.: The Global Cryosphere: Past, Present, and Future, Cambridge University Press, https://doi.org/10.1017/CBO9780511977947, 2011.

Bhuiyan, H. A., McNairn, H., Powers, J., Friesen, M., Pacheco, A., Jackson, T. J., Cosh, M. H., Colliander, A., Berg, A., Rowlandson, T., Bullock, P., and Magagi, R.: Assessing SMAP Soil Moisture Scaling and Retrieval in the Carman (Canada) Study Site, Vadose Zone Journal, 17, 1–14, https://doi.org/10.2136/vzj2018.07.0132, 2018.

Bouyoucos, G. and McCool, M. M.: A New Method of Measuring the Concentration of the Soil Solution Around the Soil Particles, Science, 42, 507–508, https://doi.org/10.1126/science.42.1084.507, 1915.

Brodzik, M. J., Billingsley, B., Haran, T., Raup, B., and Savoie, M. H.: EASE-Grid 2.0: Incremental but significant improvements for earth-gridded data sets, ISPRS International Journal of Geo-Information, 1, 32–45, https://doi.org/10.3390/ijgi1010032, 2012.

Brodzik, M. J., Billingsley, B., Haran, T., Raup, B., and Savoie, M. H.: Erratum: EASE-Grid 2.0: Incremental but significant improvements for earth-gridded data sets (ISPRS International Journal of Geo-Information (2012) 1 (32-45)), ISPRS International Journal of Geo-Information, 3, 1154–1156, https://doi.org/10.3390/ijgi3031154, 2014.

Brunet, R.: Les phénomènes de discontinuité en géographie, in: Mémoires et Documents, edited by Dresch, J., vol. 7, p. 117, Éditions du Centre national de la recherche scientifique, 1967.

Burke, H.-H. K., Bowley, C. J., and Barnes, J. C.: Determination of Snowpack Properties from Satellite Passive Microwave Measurements, Remote Sensing of Environment, 15, 1–20, https://doi.org/10.1016/0034-4257(84)90048-8, 1984.

Cheng, Q., Sun, Y., Xue, X., and Guo, J.: In Situ Determination of Soil Freezing Characteristics for Estimation of Soil Moisture Characteristics using a Dielectric Tube Sensor, Soil Science Society of America Journal, 78, 133–138, https://doi.org/10.2136/sssaj2013.03.0120n, 2014.

Choudhury, B. J. and Schmugge, T. J.: A parameterization of effective soil temperature for microwave emission., Journal of Geophysical Research, 87, 1301–1304, https://doi.org/10.1029/JC087iC02p01301, 1982.

Christensen, A. F., He, H., Dyck, M. F., Turner, E. L., Chanasyk, D. S., Naeth, M. A., and Nichol, C.: In situ measurement of snowmelt infiltration under various topsoil cap thicknesses on a reclaimed site, Canadian Journal of Soil Science, 93, 497–510, https://doi.org/10.4141/CJSS2012-048, 2013.

Colliander, A.: Calibration and Validation, in: Encyclopedia of Remote Sensing, edited by Njoku, E. G., pp. 39–46, Springer New York, https://doi.org/10.1007/978-0-387-36699-9_10, 2014.

Derksen, C., LeDrew, E., and Goodison, B.: Temporal and spatial variability of North American prairie snow cover (1988–1995) inferred from passive microwave- derived snow water equivalent imagery, Water Resources Research, 36, 255–266, https://doi.org/10.1029/1999WR900208, 2000.

https://doi.org/10.5194/egusphere-2025-3630
Preprint. Discussion started: 10 October 2025

Derksen, C., Xu, X., Dunbar, R. S., Colliander, A., Kim, Y., Kimball, J. S., Black, T. A., Euskirchen, E., Langlois, A., Loranty, M. M., Marsh, P., Rautiainen, K., Roy, A., Royer, A., and Stephens, J.: Retrieving landscape freeze/thaw state from Soil Moisture Active Passive (SMAP) radar and radiometer measurements, Remote Sensing of Environment, 194, 48–62, https://doi.org/10.1016/j.rse.2017.03.007, 2017.

Dunbar, S., Xu, X., Colliander, A., Derksen, C., Kimball, J., and Kim, Y.: Soil Moisture Active Passive (SMAP) Algorithm Theoretical Basis Document (ATBD) SMAP Level 3 Radiometer Freeze/Thaw Data Products (L3_FT_P and L3_FT_P_E), Technical report, Jet Propulsion Laboratory, Pasadena, CA, https://nsidc.org/sites/default/files/l3_ft_p_atbd_revisionc_vf.pdf, 2020.

Élise Devoie, Gruber, S., and McKenzie, J. M.: A repository of measured soil freezing characteristic curves: 1921 to 2021, Earth System Science Data, 14, 3365–3377, https://doi.org/10.5194/essd-14-3365-2022, 2022.

Entekhabi, D., Njoku, E. G., O'Neill, P. E., Kellogg, K. H., Crow, W. T., Edelstein, W. N., Entin, J. K., Goodman, S. D., Jackson, T. J., Johnson, J., Kimball, J., Piepmeier, J. R., Koster, R. D., Martin, N., McDonald, K. C., Moghaddam, M., Moran, S., Reichle, R., Shi, J. C., Spencer, M. W., Thurman, S. W., Tsang, L., and Zyl, J. V.: The soil moisture active passive (SMAP) mission, Proceedings of the IEEE, 98, 704–716, https://doi.org/10.1109/JPROC.2010.2043918, 2010.

Flerchinger, G., Lehrsch, G., and McCool, D.: Freezing and Thawing | Processes, in: Encyclopedia of Soils in the Environment, edited by Hillel, D., vol. 2, pp. 104–110, Elsevier, Ltd,, 2005.

He, H. and Dyck, M.: Application of Multiphase Dielectric Mixing Models for Understanding the Effective Dielectric Permittivity of Frozen Soils, Vadose Zone Journal, 12, vzj2012.0060, https://doi.org/10.2136/vzj2012.0060, 2013.

Holmes, T. R., Jackson, T. J., Reichle, R. H., and Basara, J. B.: An assessment of surface soil temperature products from numerical weather prediction models using ground-based measurements, Water Resources Research, 48, https://doi.org/10.1029/2011WR010538, 2012.

Hu, G., Zhao, L., Zhu, X., Wu, X., Wu, T., Li, R., Xie, C., and Hao, J.: Review of algorithms and parameterizations to determine unfrozen water content in frozen soil, Geoderma, 368, 114–277, https://doi.org/10.1016/j.geoderma.2020.114277, 2020.

Ireson, A. M., van der Kamp, G., Ferguson, G., Nachshon, U., and Wheater, H. S.: Hydrogeological processes in seasonally frozen northern latitudes: understanding, gaps and challenges, Hydrogeology Journal, 21, 53–66, https://doi.org/10.1007/s10040-012-0916-5, 2013.

Jackson, T., Colliander, A., Kimball, J., Reichle, R., Crow, W., Entekhabi, D., and O'Neil, P.: Soil Moisture Active (SMAP) Mission: Science Data Calibration and Validation Plan, Technical report, Jet Propulsion Laboratory, Pasadena, CA, https://smap.jpl.nasa.gov/files/smap2/CalVal_Plan_120706_pub.pdf, 2012.

Johnson, M. T., Ramage, J., Troy, T. J., and Brodzik, M. J.: Snowmelt Detection with Calibrated, Enhanced-Resolution Brightness Temperatures (CETB) in Colorado Watersheds, Water Resources Research, 56, https://doi.org/10.1029/2018WR024542, 2020.

Jones, L. A., Ferguson, C. R., Kimball, J. S., Zhang, K., Chan, S. T. K., McDonald, K. C., Njoku, E. G., and Wood, E. F.: Satellite Microwave Remote Sensing of Daily Land Surface Air Temperature Minima and Maxima From AMSR-E, IEEE Journal of Selected Topics in Applied Earth Observations and Remote Sensing, 3, 111–123, https://doi.org/10.1109/JSTARS.2010.2041530, 2010.

Kerr, Y. H., Mahmoodi, A., Mialon, A., Biltar, A. A., Rodríguez-Fernández, N., Richaume, P., Cabot, F., Wigneron, J. P., Waldteufel, P., Ferrazzoli, P., Schwank, M., and Delwart, S.: Soil moisture retrieval algorithms: The SMOS case, Comprehensive Remote Sensing, 1-9, 156–190, https://doi.org/10.1016/B978-0-12-409548-9.10355-0, 2017.

Kim, Y., Kimball, J. S., McDonald, K. C., and Glassy, J.: Developing a global data record of daily landscape freeze/thaw status using satellite passive microwave remote sensing, IEEE Transactions on Geoscience and Remote Sensing, 49, 949–960, https://doi.org/10.1109/TGRS.2010.2070515, 2011.

Kim, Y., Kimball, J. S., Glassy, J., and Du, J.: An extended global Earth system data record on daily landscape freeze-thaw status determined from satellite passive microwave remote sensing, Earth System Science Data, 9, 133–147, https://doi.org/10.5194/essd-9-133-2017, 2017.

https://doi.org/10.5194/egusphere-2025-3630
Preprint. Discussion started: 10 October 2025

Kim, Y., Kimball, J. S., Xu, X., Dunbar, R. S., Colliander, A., and Derksen, C.: Global Assessment of the SMAP Freeze/Thaw Data Record and Regional Applications for Detecting Spring Onset and Frost Events, Remote Sensing, 11, https://doi.org/10.3390/rs11111317, 2019.

Koopmans, R. W. R. and Miller, R. D.: Soil Freezing and Soil Water Characteristic Curves, Soil Science Society of America Journal, 30, 680–685, https://doi.org/10.2136/sssaj1966.03615995003000060011x, 1966.

Kopczynski, S. E., Ramage, J., Lawson, D., Goetz, S., Evenson, E., Denner, J., and Larson, G.: Passive microwave (SSM/I) satellite predictions of valley glacier hydrology, Matanuska Glacier, Alaska, Geophysical Research Letters, 35, https://doi.org/10.1029/2008GL034615, 2008.

Koponen, H. T. and Martikainen, P. J.: Soil water content and freezing temperature affect freeze-thaw related N 2O production in organic soil, Nutrient Cycling in Agroecosystems, 69, 213–219, https://doi.org/10.1023/B:FRES.0000035172.37839.24, 2004.

Leduc-Leballeur, M., Picard, G., Macelloni, G., Arnaud, L., Brogioni, M., Mialon, A., and Kerr, Y. H.: Influence of snow surface properties on L-band brightness temperature at Dome C, Antarctica, Remote Sensing of Environment, 199, 427–436, https://doi.org/10.1016/j.rse.2017.07.035, 2017.

Lv, S., Wen, J., Simmer, C., Zeng, Y., Guo, Y., and Su, Z.: A Novel Freeze-Thaw State Detection Algorithm Based on L-Band Passive Microwave Remote Sensing, Remote Sensing, 14, https://doi.org/10.3390/rs14194747, 2022.

Mavrovic, A., Lara, R. P., Berg, A., Demontoux, F., Royer, A., and Roy, A.: Soil dielectric characterization during freeze-Thaw transitions using L-band coaxial and soil moisture probes, Hydrology and Earth System Sciences, 25, 1117–1131, https://doi.org/10.5194/hess-25-1117-2021, 2021.

McDonald, K. C. and Kimball, J. S.: Estimation of Surface Freeze-Thaw States Using Microwave Sensors, Encyclopedia of Hydrological Sciences, https://doi.org/10.1002/0470848944.hsa059a, 2005.

Mousson, A.: Einige Thatsachen betreffend das Schmelzen und Gefrieren des Wassers, Annalen der Physik, 181, 161–174, https://doi.org/10.1002/andp.18581811002, 1858.

Njoku, E., Jackson, T., Lakshmi, V., Chan, T., and Nghiem, S.: Soil moisture retrieval from AMSR-E, IEEE Transactions on Geoscience and Remote Sensing, 41, 215–229, https://doi.org/10.1109/TGRS.2002.808243, 2003.

O'neill, P., Bindlish, R., Chan, S., Chaubell, J., Colliander, A., Njoku, E., and Jackson, T.: Soil Moisture Active Passive (SMAP) Algorithm Theoretical Basis Document Level 2 & 3 Soil Moisture (Passive) Data Products, Technical report, Jet Propulsion Laboratory, https://nsidc.org/sites/default/files/l2_sm_p_atbd_rev_g_final_oct2021_0.pdf, 2021.

ONeill, P., Chan, S., Njoku, E., Jackson, T., Bindlish, R., and Chaubell, J.: SMAP L2 Radiometer Half-Orbit 36 km EASE-Grid Soil Moisture, Version 9, https://doi.org/10.5067/K7Y2D8QQVZ4L, 2023.

O'Neill, P. E., Chan, S., Njoku, E. G., Jackson, T., Bindlish, R., and Chaubell, J.: User Guide: SMAP L3 Radiometer Global Daily 36 km EASE-Grid Soil Moisture, Version 8, Technical report, Jet Propulsion Laboratory, Boulder, CO, 2021.

Öquist, M. G., Sparrman, T., Klemedtsson, L., Drotz, S. H., Grip, H., Schleucher, J., and Nilsson, M. S.: Water availability controls microbial temperature responses in frozen soil CO2 production, Global Change Biology, 15, 2715–2722, https://doi.org/10.1111/j.1365-2486.2009.01898.x, 2009.

Pardo Lara, R., Berg, A. A., Warland, J., and Tetlock, E.: In Situ Estimates of Freezing/Melting Point Depression in Agricultural Soils Using Permittivity and Temperature Measurements, Water Resources Research, 56, 1–16, https://doi.org/10.1029/2019WR026020, 2020.

Pardo Lara, R., Berg, A., Warland, J., and Parkin, G.: Implications of measurement metrics on soil freezing curves: A simulation of freeze–thaw hysteresis, Hydrological Processes, 35, https://doi.org/10.1002/hyp.14269, 2021.

https://doi.org/10.5194/egusphere-2025-3630
Preprint. Discussion started: 10 October 2025

Piepmeier, J. R., Focardi, P., Horgan, K. A., Knuble, J., Ehsan, N., Lucey, J., Brambora, C., Brown, P. R., Hoffman, P. J., French, R. T., Mikhaylov, R. L., Kwack, E.-Y., Slimko, E. M., Dawson, D. E., Hudson, D., Peng, J., Mohammed, P. N., De Amici, G., Freedman, A. P., Medeiros, J., Sacks, F., Estep, R., Spencer, M. W., Chen, C. W., Wheeler, K. B., Edelstein, W. N., O'Neill, P. E., and Njoku, E. G.: SMAP L-Band Microwave Radiometer: Instrument Design and First Year on Orbit, IEEE Transactions on Geoscience and Remote Sensing, 55, 1954–1966, https://doi.org/10.1109/TGRS.2016.2631978, 2017.

Podest, E., McDonald, K. C., and Kimball, J. S.: Multisensor microwave sensitivity to freeze/thaw dynamics across a complex boreal landscape, IEEE Transactions on Geoscience and Remote Sensing, 52, 6818–6828, https://doi.org/10.1109/TGRS.2014.2303635, 2014.

Pulliainen, J.: Mapping of snow water equivalent and snow depth in boreal and sub-arctic zones by assimilating space-borne microwave radiometer data and ground-based observations, Remote Sensing of Environment, 101, 257–269, https://doi.org/10.1016/j.rse.2006.01.002, 2006.

Ramage, J. M. and Isacks, B. L.: Determination of melt-onset and refreeze timing on southeast Alaskan icefields using SSM/I diurnal amplitude variations, Annals of Glaciology, 34, 391–398, https://doi.org/10.3189/172756402781817761, 2002.

Ramage, J. M., McKenney, R. A., Thorson, B., Maltais, P., and Kopczynski, S. E.: Relationship between passive microwave-derived snowmelt and surface-measured discharge, Wheaton River, Yukon Territory, Canada, Hydrological Processes, 20, 689–704, https://doi.org/10.1002/hyp.6133, 2006.

Rautiainen, K., Lemmetyinen, J., Pulliainen, J., Vehvilainen, J., Drusch, M., Kontu, A., Kainulainen, J., and Seppänen, J.: L-band radiometer observations of soil processes in boreal and subarctic environments, IEEE Transactions on Geoscience and Remote Sensing, 50, 1483–1497, https://doi.org/10.1109/TGRS.2011.2167755, 2012.

Rautiainen, K., Lemmetyinen, J., Schwank, M., Kontu, A., Ménard, C. B., Mätzler, C., Drusch, M., Wiesmann, A., Ikonen, J., and Pulliainen, J.: Detection of soil freezing from L-band passive microwave observations, Remote Sensing of Environment, 147, 206–218, https://doi.org/10.1016/j.rse.2014.03.007, 2014.

Rautiainen, K., Parkkinen, T., Lemmetyinen, J., Schwank, M., Wiesmann, A., Ikonen, J., Derksen, C., Davydov, S., Davydova, A., Boike, J., Langer, M., Drusch, M., and Pulliainen, J.: SMOS prototype algorithm for detecting autumn soil freezing, Remote Sensing of Environment, 180, 346–360, https://doi.org/10.1016/j.rse.2016.01.012, 2016.

Rees, W. G.: Physical Principles of Remote Sensing, Cambridge University Press, 2 edn., https://doi.org/10.1017/CBO9780511812903, 2001.

Rowlandson, T. L., Berg, A. A., Roy, A., Kim, E., Lara, R. P., Powers, J., Lewis, K., Houser, P., McDonald, K., Toose, P., Wu, A., Marco, E. D., Derksen, C., Entin, J., Colliander, A., Xu, X., and Mavrovic, A.: Capturing agricultural soil freeze/thaw state through remote sensing and ground observations: A soil freeze/thaw validation campaign, Remote Sensing of Environment, 211, 59–70, https://doi.org/10.1016/j.rse.2018.04.003, 2018.

Roy, A., Royer, A., Derksen, C., Brucker, L., Langlois, A., Mialon, A., and Kerr, Y. H.: Evaluation of Spaceborne L-Band Radiometer Measurements for Terrestrial Freeze/Thaw Retrievals in Canada, IEEE Journal of Selected Topics in Applied Earth Observations and Remote Sensing, 8, 4442–4459, https://doi.org/10.1109/JSTARS.2015.2476358, 2015.

Royer, A., Roy, A., Montpetit, B., Saint-Jean-Rondeau, O., Picard, G., Brucker, L., and Langlois, A.: Comparison of commonly-used microwave radiative transfer models for snow remote sensing, Remote Sensing of Environment, 190, 247–259, https://doi.org/10.1016/j.rse.2016.12.020, 2017.

Salmabadi, H., Pardo Lara, R., Berg, A., Mavrovic, A., and Hanes, C.: Improving Seasonally Frozen Ground Monitoring Using Soil Freezing Characteristic Curve in Permittivity-Temperature Space, The Cryosphere, Under Review.

https://doi.org/10.5194/egusphere-2025-3630
Preprint. Discussion started: 10 October 2025

Schmugge, T. J., Kustas, W. P., Ritchie, J. C., Jackson, T. J., and Rango, A.: Remote sensing in hydrology, Advances in Water Resources, 25, 1367–1385, https://doi.org/10.1016/S0309-1708(02)00065-9, 2002.

Spaans, E. J. A. and Baker, J. M.: The Soil Freezing Characteristic: Its Measurement and Similarity to the Soil Moisture Characteristic, Soil Science Society of America Journal, 60, 13–19, https://doi.org/10.2136/sssaj1996.03615995006000010005x, 1996.

Takala, M., Pulliainen, J., Metsamaki, S. J., and Koskinen, J. T.: Detection of snowmelt using spaceborne microwave radiometer data in Eurasia from 1979 to 2007, IEEE Transactions on Geoscience and Remote Sensing, 47, 2996–3007, https://doi.org/10.1109/TGRS.2009.2018442, 2009.

Takala, M., Luojus, K., Pulliainen, J., Derksen, C., Lemmetyinen, J., Kärnä, J.-P., Koskinen, J., and Bojkov, B.: Estimating northern hemisphere snow water equivalent for climate research through assimilation of space-borne radiometer data and ground-based measurements, Remote Sensing of Environment, 115, 3517–3529, https://doi.org/https://doi.org/10.1016/j.rse.2011.08.014, 2011.

Tetlock, E., Toth, B., Berg, A., Rowlandson, T., and Ambadan, J. T.: An 11-year (2007-2017) soil moisture and precipitation dataset from the Kenaston Network in the Brightwater Creek basin, Saskatchewan, Canada, Earth System Science Data, 11, 787–796, https://doi.org/10.5194/essd-11-787-2019, 2019.

Tian, H., Wei, C., Lai, Y., and Chen, P.: Quantification of Water Content during Freeze-Thaw Cycles: A Nuclear Magnetic Resonance Based Method, Vadose Zone Journal, 17, 160 124, https://doi.org/10.2136/vzj2016.12.0124, 2018.

Tilston, E. L., Sparrman, T., and Öquist, M. G.: Unfrozen water content moderates temperature dependence of sub-zero microbial respiration, Soil Biology and Biochemistry, 42, 1396–1407, https://doi.org/10.1016/j.soilbio.2010.04.018, 2010.

Ulaby, F. T., Moore, R. K., and Fung, A. K.: Microwave remote sensing: Fundamentals and radiometry v. 1, Remote sensing library, Artech House, Norwood, MA, 1981.

Vuyovich, C. and Jacobs, J. M.: Snowpack and runoff generation using AMSR-E passive microwave observations in the Upper Helmand Watershed, Afghanistan, Remote Sensing of Environment, 115, 3313–3321, https://doi.org/10.1016/j.rse.2011.07.014, 2011.

Wagner-Riddle, C., Congreves, K. A., Abalos, D., Berg, A. A., Brown, S. E., Ambadan, J. T., Gao, X., and Tenuta, M.: Globally important nitrous oxide emissions from croplands induced by freeze-thaw cycles, Nature Geoscience, 10, 279–283, https://doi.org/10.1038/ngeo2907, 2017.

Wen, Z., Ma, W., Feng, W., Deng, Y., Wang, D., Fan, Z., and Zhou, C.: Experimental study on unfrozen water content and soil matric potential of Qinghai-Tibetan silty clay, Environmental Earth Sciences, 66, 1467–1476, https://doi.org/10.1007/s12665-011-1386-0, 2012.

Wigneron, J.-P., Chanzy, A., Calvet, J.-C., and Bruguier, N.: A simple algorithm to retrieve soil moisture and vegetation biomass using passive microwave measurements over crop fields, Remote Sensing of Environment, 51, 331–341, https://doi.org/10.1016/0034-4257(94)00081-W, 1995.

Williamson, M., Rowlandson, T. L., Berg, A. A., Roy, A., Toose, P., Derksen, C., Arnold, L., and Tetlock, E.: L-band radiometry freeze/ thaw validation using air temperature and ground measurements, Remote Sensing Letters, 9, 403–410, https://doi.org/10.1080/2150704X.2017.1422872, 2018.

Xu, J., Wen, X., Zhang, H., Luo, D., Xu, L., and Wu, Z.: Multi-scale characteristics of remote sensing lineaments, Earth Science Informatics, 13, 287–297, https://doi.org/10.1007/s12145-019-00430-y, 2020.

Xu, X., Derksen, C., Yueh, S. H., Dunbar, R. S., and Colliander, A.: Freeze/Thaw Detection and Validation Using Aquarius' L-Band Backscattering Data, IEEE Journal of Selected Topics in Applied Earth Observations and Remote Sensing, 9, 1370–1381, https://doi.org/10.1109/JSTARS.2016.2519347, 2016.

https://doi.org/10.5194/egusphere-2025-3630
Preprint. Discussion started: 10 October 2025

Xu, X., Dunbar, R., Derksen, C., Colliander, A., Kim, Y., and Kimball, J.: SMAP L3 Radiometer Global and Northern Hemisphere Daily 36 km EASE-Grid Freeze/Thaw State, Version 4, https://doi.org/10.5067/LQQ5I3QVGFTU, 2023.

Yoshikawa, K. and Overduin, P. P.: Comparing unfrozen water content measurements of frozen soil using recently developed commercial sensors, Cold Regions Science and Technology, 42, 250–256, https://doi.org/10.1016/j.coldregions.2005.03.001, 2005.

Zhou, Y., Zhou, J., you Shi, X., and qing Zhou, G.: Practical models describing hysteresis behavior of unfrozen water in frozen soil based on similarity analysis, Cold Regions Science and Technology, 157, 215–223, https://doi.org/10.1016/j.coldregions.2018.11.002, 2019.